CASE FILE
COPY

RM A56B21

NACA RM A56B21

NACA

RESEARCH MEMORANDUM

LIGHT DIFFUSION THROUGH HIGH-SPEED TURBULENT BOUNDARY LAYERS

By Howard A. Stine and Warren Winovich

Ames Aeronautical Laboratory
Moffett Field, Calif.

NATIONAL ADVISORY COMMITTEE
FOR AERONAUTICS

WASHINGTON

May 25, 1956
Declassified February 26, 1958

47

NATIONAL ADVISORY COMMITTEE FOR AERONAUTICS

RESEARCH MEMORANDUM

LIGHT DIFFUSION THROUGH HIGH-SPEED TURBULENT BOUNDARY LAYERS

By Howard A. Stine and Warren Winovich

SUMMARY

The optical transmission characteristics of turbulent boundary layers in air on a flat plate with negligible heat transfer were measured photometrically for ranges of Mach number from 0.4 to 2.5. Free-stream densities and boundary-layer thicknesses ranged, respectively, from 0.12 to 0.93 standard sea-level atmospheres and from 1-1/2 to 3-1/2 inches.

It was found empirically that the scattering from a collimated beam of white light which penetrates a turbulent boundary layer depends mainly upon the integral across the layer of the difference between the free-stream density and the local boundary-layer density. The radiant power scattered thus appears to be dependent both upon density fluctuations proportional to the change in mean density across the boundary layer and to an integral scale of the density fluctuations proportional to the boundary-layer thickness. The scattered light is deviated in all cases through very small angles, the maximum in these tests being about 0.0006 radian measured from the direction of primary propagation. The distribution of energy in the scattered field depends mainly upon the integral scale of the density fluctuations and is in excellent agreement with a theoretical prediction based on the scattering cross section of Booker and Gordon. Comparisons of scattered patterns through two boundary layers with those through four show small deviations from Lambert's exponential law. These differences are attributed both to secondary scattering and to diffuse refraction at the boundary-layer free-stream interfaces.

The results show that significant deterioration in resolving power can be sustained by optical imaging devices which receive radiant energy through compressible turbulent boundary layers. For example, the included angle between two equally bright point objects which can just be resolved by a 2-1/2-inch objective is about 2 seconds of arc. If this objective looks through a 1-3/4-inch-thick turbulent boundary layer at a Mach number of 2.5 and a density altitude of 45,000 feet, this angle increases to about 8 seconds of arc.

The results, moreover, show that photometric measurements in the radiation field produced by the interaction of a plane light wave with a turbulent boundary layer can be used in conjunction with scattering theory to deduce average values of the integral scale and the intensity of turbulent density fluctuations.

INTRODUCTION

Due to the process of scattering (or diffusion), the quality of optical images received aboard an airborne vehicle traveling at high speed can be expected to deteriorate if the radiation traverses a turbulent boundary layer. The subjective effect of this deterioration can be likened to the common sensation brought about when one views a distant object over a hot chimney and observes a general blurring of outline and disappearance of fine detail. It is obvious that airborne optical devices, such as reconnaissance cameras, star-tracking telescopes, and fire-control sights can be similarly affected by high-speed turbulent boundary layers, and thus will suffer a loss in resolving power.

A qualitative insight into the optical scattering ability of turbulent boundary layers can be gained by reference to figure 1 which shows two shadow photographs of identical bodies in the Ames supersonic free flight wind tunnel (ref. 1) at comparable Mach numbers and Reynolds numbers. Both photographs were obtained with an electric spark illumination of 0.5 microsecond, and differ in that the body of figure 1(a) was launched through still air whereas the body shown in figure 1(b) was launched into a counterflow at a Mach number of 2. Thus, the light which exposed the film of figure 1(b) penetrated two turbulent boundary layers on the wind-tunnel side walls, and therein was refracted by the turbulent density fluctuations in such a manner as to cause the background to take on the mottled, grain-like pattern shown. Because of the great difference between the speed of light and the speed of the turbulent eddies and because the spark duration was sufficiently short, the turbulent motion was "stopped" in the pattern shown. However, during a finite time interval the pattern will, of course, change and each ray of light which enters the turbulence at a given point will illuminate, in the course of time, a finite area upon emergence. Thus, a one-to-one correspondence between entering and emerging light rays is lost, because, in effect, the turbulence introduces a random noise field in the primary beam.

Using linearized theory of geometrical optics, Liepmann (ref. 2) has estimated the rms diffusion angle of a ray for various flight conditions. A more detailed scattering analysis based on the electromagnetic theory of radiation and the theory of isotropic turbulence has been advanced by Booker and Gordon, and refined by Villars and Weisskopf (refs. 3 and 4). Baskins and Hamilton (refs. 5 and 6) have measured the transmission characteristics of turbulent boundary layers for a limited range of flow

conditions. The results of these theoretical and experimental studies show that a significant loss in resolving power can be sustained by optical imaging equipment receiving radiant energy which has penetrated a high-speed turbulent boundary layer.

The purpose of the present experimental investigation is to provide additional data on the optical transmission characteristics of turbulent boundary layers over a range of Mach numbers from 0.4 to 2.5, free-stream densities from 0.12 to 0.93 standard sea-level atmospheres, and boundary-layer thicknesses from 1-1/2 to 4-1/2 inches and to correlate the observed optical characteristics with the appropriate boundary-layer parameters.

NOTATION

C Gladstone-Dale constant (0.1170 ± 0.0002 cu ft/slug for air and 5200 A light)

d focal plane stop diameter, ft

D entrance pupil diameter, ft

E radiant intensity averaged with respect to time, watts/sq ft

f/no. focal ratio, $\frac{F}{D}$, dimensionless

F focal length, ft

I time-averaged radiant intensity at the focal plane of telephotometer, watts/sq ft

K beam-spread parameter, $\left(\frac{4\pi l}{\lambda}\right)^2$, dimensionless

l integral scale of density fluctuations, ft

M Mach number, dimensionless

N index of refraction, $1 + C\rho$, dimensionless

n number of boundary layers traversed

P radiant flux (power), watts

p pressure, ρRT, lb/sq ft

R gas constant, 1715 sq ft/sec^2 $^\circ$F, for air

r radius normal to optical axis of telephotometer with origin at the principal focus, ft

T temperature, $\dfrac{T_t}{1 + (\gamma - 1)M^2/2}$, $^\circ$R

u air velocity, ft/sec

y distance through boundary layer normal to surface, ft

α attenuation coefficient, 1/ft

β boundary-layer correlating parameter (eq. (25)), dimensionless

γ specific heat ratio, 1.4 for air, dimensionless

δ boundary-layer thickness, ft

ϵ specific inductive capacity, dielectric constant, N^2, for air, dimensionless

θ scattering angle measured from direction of primary propagation, radians

θ_M angular aperture of telephotometer, $\tan^{-1}\dfrac{d}{2F}$, radians

λ radiation wave length, ft

$\bar{\lambda}$ effective radiation wave length, 1.705×10^{-6} ft

ξ dimensionless radius normal to optical axis of telephotometer, $\dfrac{\pi Dr}{F\bar{\lambda}}$

ρ air density, slugs/cu ft

$\bar{\rho}$ density of NACA standard sea-level air, 0.002378 slug/cu ft

σ scattering cross section per unit volume, sq ft/cu ft steradian

φ angle of incidence measured from normal to flow direction, deg

χ angle between direction of electric vector and scattering direction θ, radians

ω solid angle, steradians

Subscripts

A	absorbed
B	boundary layer
F	flow
M	measured
NF	no flow
n	number of boundary layers, for example, 1, 2, or 4
o	incident
P	polarized
R	Rayleigh
S	scattered
sep	separated region of boundary layer
t	stagnation
U	unpolarized
∞	free stream

ANALYSIS

Attenuation of Light in Turbid Media

Aggregations of particulate matter, such as air, smoke in air, liquid emulsions, colloidal suspensions, etc., are known to attenuate a beam of parallel monochromatic light in close accord with Lambert's exponential law for homogeneous media (refs. 7, 8, and 9). This law states that layers of equal thickness attenuate equal fractions of the incident intensity. In differential form the law is written

$$\frac{dE}{E} = -\alpha \, dy \tag{1}$$

The attenuation per foot of penetration, α, is a function of the vibration frequency and state of polarization of the incident light, the structure,

both atomic and macroscopic, of the particles, and, above all, of the degree of chaos (random fluctuations) in the particle number density. Ordinarily, α is considered to be made up of two parts, an absorption coefficient, α_A, and a scattering coefficient, α_S, to distinguish between the intensity decrease due to disappearance of visible light into radiation at other frequencies, such as heat, and that due to deflection of visible energy from the direction of primary propagation. It is the latter which is affected by turbulent density fluctuations in air.

In the application of equation (1) to the boundary layer, the attenuation per foot due to scattering, α_S, cannot be taken as a constant, but must be considered as a function of position because the boundary layer is an inhomogeneous medium. However, insofar as a turbulent boundary layer can be considered an assembly of particles, it might be expected that equation (1) would describe the optical transmission characteristics of a series of identical boundary layers, each having an average scattering coefficient $\bar{\alpha}_S$ and thickness δ. Such a definition is:

$$\left(\frac{E}{E_O}\right)_n = \left(e^{-\bar{\alpha}_S \delta}\right)^n \tag{2}$$

where n denotes the number of boundary layers traversed. Equation (2) forms a starting point for the experimental procedure used in the present investigation because it provides a method for deducing, from the results of observations through a multiplicity of identical boundary layers, the transmission characteristics of a single boundary layer. In particular, the relations between four, two, and one identical boundary layers are

$$\left(\frac{E}{E_O}\right)_4 = \left(\frac{E}{E_O}\right)_2^2 = \left(\frac{E}{E_O}\right)_1^4 \tag{3}$$

It should be noted that this result is due to the functional form of Lambert's law and that nothing need be known about the scattering coefficient and the thickness of the scattering medium, so long as the several media are identical and contiguous.

Attenuation of Light by Isotropic Density Fluctuations

Lack of knowledge of the turbulence structure in a compressible turbulent boundary layer precludes the calculation of α_S in general. However, the attenuation of electromagnetic waves due to scattering by turbulence can be calculated for a turbulence model characterized by

isotropic density fluctuations having an exponentially decaying autocorrelation function. The calculation utilizes the scattering cross section for this model deduced by Booker and Gordon (ref. 3), the turbulence structure being defined solely by two parameters, namely, intensity and integral scale of the density fluctuations.

One might argue against the worth of such a calculation on two counts. First, the turbulence model of Booker and Gordon is physically unrealistic because the exponentially decaying autocorrelation function implies that the turbulence has no microscale. Second, a two-parameter model of isotropic turbulence cannot be expected adequately to describe the anisotropic inhomogeneous turbulence anticipated in compressible turbulent boundary layers. The extent to which scatter propagation is influenced by these discrepancies between the turbulence model of Booker and Gordon and more refined models involving three or more parameters has been discussed by Wheelon, Muchmore and Wheelon, and Staras in references 10, 11, and 12. Whereas these investigations show that the Booker and Gordon scattering cross section is, of course, altered by choice of correlation function and considerations of anisotropy, the absolute changes in cross section are small for large arbitrary changes in the turbulence model. One is therefore encouraged to believe that the relatively simple calculations based on the results of the Booker and Gordon analysis can, at the very least, point out the significant variables and aid in the analysis of data.

The radiant flux (power) scattered by isotropic density fluctuations per unit solid angle, per unit incident intensity, per unit macroscopic element of volume as given by Booker and Gordon is

$$\sigma_p = \frac{\overline{\left(\frac{\Delta\epsilon}{\epsilon}\right)^2} \frac{(2\pi l)^3}{\lambda^4}}{\left[1 + \left(\frac{4\pi l}{\lambda}\right)^2 \sin^2 \frac{\theta}{2}\right]^2} \sin^2 \chi \qquad (4)$$

This equation states that the fraction of incident radiant power scattered into unit solid angle per foot of penetration through the turbulence, σ_p, is directly proportional to the mean square fractional fluctuation of the specific inductive capacity of the medium ϵ (and thus to the density fluctuations);[1] directly proportional to the cube of the characteristic

[1]Using definitions given in the NOTATION, which apply to dry air:

$$\overline{\left(\frac{\Delta\epsilon}{\epsilon}\right)^2} = 4\overline{\left(\frac{\Delta N}{N}\right)^2} \doteq 4C^2\overline{(\Delta\rho)^2} \quad \text{for} \quad C\rho << 1$$

size of the density "lumps" (integral scale of turbulence), l; and inversely proportional to the fourth power of the radiation wave length, λ. The dependence of the scattered power on angle is contained both in the denominator of equation (4), where the polar angle, θ, is measured from the direction of primary propagation, and in the term $\sin^2\chi$ in the numerator, where χ is the angle between the direction of the polarized incident electric vector and the scattering direction θ. Equation (4) can be modified so as to be applicable to natural (unpolarized) incident light by replacing the term $\sin^2\chi$ by the term $1/2(1 + \cos^2\theta)$ (ref. 13). Then

$$\sigma_U = \frac{\overline{\left(\frac{\Delta\epsilon}{\epsilon}\right)^2}\,\frac{(2\pi l)^3}{\lambda^4}}{\left[1 + \left(\frac{4\pi l}{\lambda}\right)^2 \sin^2\frac{\theta}{2}\right]^2}\left(\frac{1 + \cos^2\theta}{2}\right) \tag{5}$$

From equation (5) it can be seen that, in addition to being symmetrical about the propagation axis, the power distribution in the scattered field for an unpolarized plane incident wave is strongly dependent on the comparative magnitudes of the integral scale l and the wave length λ. In fact, when l is very much greater than λ, which appears to be the relevant case for visible light and turbulent boundary layers, and since the half-power point of the scattered beam makes an angle of $\lambda/4\pi l$ with the propagation axis, the scattering takes place mainly in the forward direction.

Using equation (5), one further concludes that a layer consisting of isotropic density fluctuations of macroscopic thickness dy and unit cross-section area scatters the fraction of incident power:[2]

$$\alpha_S dy = \left[\int_0^{4\pi} \sigma_U(\omega,y)\,d\omega\right] dy \tag{6}$$

Thus, for negligible absorption, the attenuation suffered by the primary beam due to scattering in penetrating the isotropic turbulent medium a distance y becomes (eqs. (1) and (6)):

[2]The analysis of Villars and Weisskopf (ref. 4), which employs a turbulence model based on Kolmogoroff's concept of local isotropy, yields a scattering cross section which is not defined along the direction of primary propagation. Thus, their function cannot be used as the integrand in equation (6).

$$\frac{E}{E_o} = e^{-\int_o^y \int_o^{4\pi} \sigma_U d\omega \, dy} \tag{7}$$

Because of assumptions evoked by Booker and Gordon in the derivation of σ, equation (7) is rigorously valid only for cases where an element of thickness of the turbulent stratum dy exceeds the integral scale l. In other words, the turbulence must be sensibly homogeneous throughout the volume $(dy)^3$. Further, the total thickness of the turbulent layer, y, must exceed the radiation wave length, λ. Finally, it should be noted that the effects of multiple scattering have been neglected.

Measurement of Light Intensity in Scattered Field

It is known (refs. 14 and 15, for example) that photometric experiments involving Lambert's law can be subject to error because it is impossible to restrict the angular aperture of the measuring instrument to zero. Thus, an instrument centered on the axis of primary propagation and situated a finite distance from the scattering volume gathers, in addition to the attenuated plane wave, that portion of the scattered light lying within its field of view. To account for this effect, equation (7) is modified to read:

$$\frac{E_M}{E_o} = e^{-\int_o^{y=\delta} \int_{\omega_M}^{4\pi} \sigma_U d\omega \, dy} \tag{8}$$

where E_M is the intensity measured by an instrument having a field of view defined by the solid angle ω_M. The instrument is considered located sufficiently far from the scattering layer that changes in solid angle with layer depth can be neglected. (This is the paraxial ray assumption of geometrical optics.) For an instrument with an axially symmetric field of view alined with the axis of primary propagation, the solid angle subtended, ω, is related to the scattering angle, θ, by

$$\omega \equiv 4\pi \sin^2 \frac{\theta}{2} \equiv 2\pi(1 - \cos \theta) \tag{9}$$

After the foregoing equalities are used to effect substitutions in equation (5), the angular integration indicated in the exponent of equation (8) can be carried out by elementary methods. The result is:

$$\alpha_{SM} = \int_{\omega_M}^{4\pi} \sigma_U d\omega = \frac{(2\pi l)^3}{\lambda^4} \overline{\left(\frac{\Delta\epsilon}{\epsilon}\right)^2} \left\{ \frac{K}{1+K} \left(\frac{1 - \frac{\omega_M}{4\pi}}{1 + \frac{K\omega_M}{4\pi}} \right) \left[\frac{4\pi}{K} + \frac{1}{2\pi}\left(\frac{4\pi}{K}\right)^2 + \frac{1}{8\pi^2}\left(\frac{4\pi}{K}\right)^3 \right] + \right.$$

$$\left. \frac{K}{8\pi^2}\left(\frac{4\pi}{K}\right)^3 \left(1 - \frac{\omega_M}{4\pi}\right) + \left[\frac{1}{2\pi}\left(\frac{4\pi}{K}\right)^2 + \frac{1}{4\pi^2}\left(\frac{4\pi}{K}\right)^3 \right] \ln \left(\frac{1 + \frac{K\omega_M}{4\pi}}{1+K} \right) \right\} \tag{10}$$

where $K = (4\pi l/\lambda)^2$. The scattering coefficient α_S (eq. (6)) corresponds to equation (10) with $\omega_M = 0$.

In the case of velocity fluctuations (refs. 16, 17, and 18), it has been found that the integral scale is of the order of half the boundary-layer thickness. It is reasonable to expect that the scale of the density fluctuations will be of a similar order of magnitude, say about 1 inch, for flight and wind-tunnel boundary layers. Because the wave length of yellow light is about 2×10^{-5} inch, the discussion can therefore be restricted to cases where l is very much greater than λ. Consequently, only the leading term of equation (10) contributes significantly to the scattering coefficient, and one obtains with the help of equation (9):

$$\left.\begin{aligned} \alpha_{SM} &\doteq \frac{2\pi^2 l}{\lambda^2} \overline{\left(\frac{\Delta\epsilon}{\epsilon}\right)^2} \left[\frac{1 - \sin^2 \frac{\theta_M}{2}}{1 + \left(\frac{4\pi l}{\lambda}\right)^2 \sin^2 \frac{\theta_M}{2}} \right] \\ \text{and, for } \theta_M = 0: \quad \alpha_S &\doteq \frac{2\pi^2 l}{\lambda^2} \overline{\left(\frac{\Delta\epsilon}{\epsilon}\right)^2} \end{aligned}\right\} \tag{11}$$

Furthermore, the results of references 16 and 18 indicate that the integral scale of the velocity fluctuations is, for practical purposes, independent of position in the boundary layer. When it is assumed that the integral scale of the density fluctuations is likewise independent of position, the integration with respect to distance indicated in equation (8) yields:

$$\left.\begin{aligned} \ln\left(\frac{E_M}{E_O}\right) &= -\left[\frac{1 - \sin^2\frac{\theta_M}{2}}{1 + \left(\frac{4\pi l}{\lambda}\right)^2 \sin^2\frac{\theta_M}{2}}\right] \frac{2\pi^2 l}{\lambda^2} \int_O^{y=\delta} \overline{\left(\frac{\Delta\epsilon}{\epsilon}\right)^2}\, dy \\ \text{and, for } \theta_M = 0: \quad \ln\left(\frac{E}{E_O}\right) &= -\frac{2\pi^2 l}{\lambda^2} \int_O^{y=\delta} \overline{\left(\frac{\Delta\epsilon}{\epsilon}\right)^2}\, dy \end{aligned}\right\} \quad (12)$$

The first of equations (12) relates the measured intensity ratio E_M/E_O for given wave length of the incident radiation and structure of the turbulence as characterized by integral scale and intensity of density fluctuations with the changes in angular aperture, θ_M, of the viewing instrument. These results are applicable to turbulent compressible boundary layers subject to the following qualifications: (1) the integral scale is considered invariant throughout the layer; (2) the integral scale is very much greater than the radiation wave length; (3) the turbulence can be considered isotropic; and (4) the turbulence is characterized by a space correlation of the density fluctuations that obeys an exponential decay law.

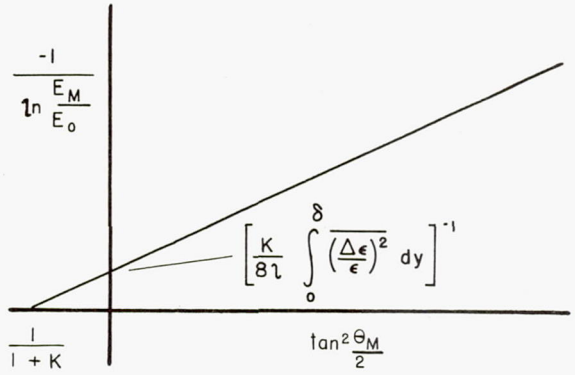
Photometric Exploration of Fluctuating Density Fields

Although the foregoing analysis presumes that the integral scale and intensity of the density fluctuations are known and the radiation intensity is the dependent variable, the converse is usually true in practice. It is therefore convenient also to regard equations (12) as defining the turbulence structure in terms of known radiation variables, thereby permitting the extraction of useful information about turbulent layers. To this end the first of equations (12) can be rearranged to read:

$$-\frac{1}{\ln\left(\frac{E_M}{E_o}\right)} = \frac{1}{\frac{2\pi^2 l}{\lambda^2}\int_o^{y=\delta}\overline{\left(\frac{\Delta\epsilon}{\epsilon}\right)^2}\,dy} + \frac{1+\left(\frac{4\pi l}{\lambda}\right)^2}{\frac{2\pi^2 l}{\lambda^2}\int_o^{y=\delta}\overline{\left(\frac{\Delta\epsilon}{\epsilon}\right)^2}\,dy}\tan^2\frac{\theta_M}{2} \qquad (13)$$

It appears from equation (13) that photometric surveys of the light field after interaction with the turbulent layer, wherein the ratio E_M/E_o is measured as the angular aperture θ_M of the photometer is varied, can yield values of the unknown turbulent parameters l and $\int_o^{y=\delta}\overline{\left(\frac{\Delta\epsilon}{\epsilon}\right)^2}\,dy$.

This is true because a graph of the left-hand side of equation (13) against the aperture function on the right-hand side yields determinate functions of the unknowns as the slope and intercept of a straight line (sketch (a)).



Sketch (a)

As part of the present investigation, the functional adequacy of equations (12) and (13) when applied to turbulent compressible boundary layers was tested by comparison with photometric data.

APPARATUS AND PROCEDURE

Wind Tunnel

The present experimental investigation was conducted in the Ames 1- by 3-foot supersonic wind tunnel no. 1. The natural boundary layers that exist on the tunnel side walls were thickened artificially to obtain a range of test conditions. This closed circuit, continuous operation, variable pressure wind tunnel is equipped with a flexible-plate nozzle that provides a range of supersonic Mach numbers from 1.20 to 2.50. A

range of subsonic Mach numbers from 0.40 to 0.85 can also be provided at the test section by locating the minimum area in the circuit downstream of the test section.

The working fluid is dry, filtered, atmospheric air. Contamination within the circuit due to oil and manometer fluid vapors and leaks from the atmosphere is minimized by continuous air interchange at a rate sufficient to prevent water condensation in the nozzle. The absolute pressure in the settling chamber can be varied from 1/5 atmosphere to 2 atmospheres to provide changes in Reynolds number. Corresponding absolute temperatures vary from 520° R to 600° R and depend primarily upon the absolute pressure. Stagnation pressure and stagnation temperature can be measured with a relative error of ±1 percent in the most uncertain cases.

Some heat flow always takes place between the room and the nozzle boundary layers, but the heat-transfer rates are small. This is manifested by the fact that the wall temperatures have equilibrium values within a degree or two of the theoretical recovery temperatures of the stream. The temperatures on the test-section wall vary from about 20° F above room temperature at the lowest Mach number and highest pressure to about 25° F below room temperature at the highest Mach number and lowest pressure. Although it is usually possible to select a stagnation pressure which produces zero heat transfer at any given Mach number, it was felt that a close control of heat transfer was unwarranted because the heat flow rates are small.

Instrumentation

Aerodynamic.- Boundary-layer pressure data were provided by either a 28-tube or a 36-tube total-pressure rake which spanned the test section on the horizontal median plane, 4-5/8 inches downstream from the center of the 9-inch-diameter viewing windows (fig. 2), and also by 25 static-pressure orifices on each test-section wall. Pressures were indicated by a conventional liquid manometer system. In addition, three hot-wire anemometer probes were installed at the rake station with the wires normal to the air stream. One probe was mounted integrally with the rake on the wind-tunnel axis. The remaining two were installed on a horizontal traversing mechanism so that they could be traversed through the boundary layers on opposite walls of the wind tunnel. The hot-wire anemometer was used for obtaining relative boundary-layer and free-stream turbulence levels and for detecting the location of the edges of the boundary layers.

The relative error in determining Mach number from the rake total head and wall static pressure is ±1 percent. Locations of the centers of the 1/32 inch outside diameter total head tubes were measured to the nearest 1/64 inch.

Optical.- The optical equipment used in the present investigation was substantially the same as that employed by Baskins and Hamilton (refs. 5 and 6). The principal components were three identical f/8.6 Newtonian telescopes having focal lengths of 21.45 inches. Two of the telescopes were used as source collimators, and the remaining instrument was equipped as a telephotometer. Light from battery-operated tungsten-filament incandescent bulbs was relayed to 0.00025-inch-diameter apertures at the principal foci of each collimator. Electronic photometers viewing the sources directly served as monitors of the two source intensities. As is shown in figure 2 a collimator was arranged on each side of the wind tunnel to direct, as required, plane waves toward either of the high-quality windows (see ref. 6 for description) in the wind-tunnel side walls. A half-silvered mirror and the receiving telescope were situated on opposite sides of the wind tunnel so that some of the radiant energy from either collimator could enter the receiver after passing either once or twice through the air stream.[3] After passing through the final wind-tunnel window, light from the selected collimator entered the receiver through a plane-parallel glass plate which capped the telescope barrel at an angle of 45° with respect to the optical axis. The reflex mirror which is characteristic of the Newtonian arrangement was situated at the center of this plate and consisted of an elliptical deposit of aluminum having a nominal minor diameter of 1/4 inch. Thus the entrance pupil was an annular window having a nominal major diameter of 2-1/2 inches and a nominal minor diameter of 1/4 inch, and the resulting diffraction pattern at the principal focus was of the center-blocked Airy type. Although the source diameter was not sufficiently small to meet the rather strict coherence criterion of Hopkins (ref. 19), it was about one-half the maximum diameter considered adequate by Gabor (ref. 20) and two-thirds the diameter considered a good working compromise by Rogers (ref. 21).

The receiving telescope was equipped with means for inserting at the principal focus a series of pinhole apertures having diameters ranging from 0.0007 to 0.0330 inch. When in position, the center of each pinhole

[3]Because the receiver and source collimator on the same side of the tunnel were physically separated, the double-transmission beam incident on the mirror irradiated slightly different portions of the boundary layers before than it did after reflection toward the receiver. The maximum displacement between incident and reflected beams was about 1 inch at the surface of the near window.

The original optical arrangement for the double-transmission tests employed an opaque first-surface mirror which could be inserted at the location of the half-silvered mirror. Because installation and calibration became a lengthy and frequently repeated process, and because the wind tunnel had to be shut down during changes from single-transmission to double-transmission operation, the arrangement using the half-silvered mirror proved to be the more desirable from an operational standpoint.

coincided with the optical axis of the receiver. The radiation which passed each pinhole was relayed by a lens system as a collimated beam to a 1/8-inch-diameter spot on the cathode of a 1P21 photomultiplier tube. The photomultiplier tube acted as the transducer of a commercially available indicating photometer. Repeated calibrations on an optical bench showed that this instrument was stable with time and had a linear response within about 0.5 percent of full scale for output readings below 15 microamperes. The combination of light source, optical components, and photoelectric cell possessed a spectral sensitivity having a maximum response at a wave length of about 5200 angstrom units. The energy intercepted by the phototube was measured with a maximum relative error of ±2 percent.

With the various pinholes in place, the angular aperture of the photocell varied from 1.7×10^{-5} to 7.7×10^{-4} radian. Aperture diameters were measured to the nearest 0.00001 inch, which corresponds to slightly less than 0.03×10^{-5} radian in angular aperture. Angular apertures corresponding to the various pinholes are recorded in table I.

The collimators and telephotometer were mounted on a cradle which was isolated from the floor and the tunnel structure by an elastic cord suspension. The cradle assembly and test section were housed in a cabin to minimize extraneous illumination and room turbulence.

Tests

Aerodynamic parameters.- In addition to the individual effects of Mach number and free-stream density on the diffusion of light, the effect of boundary-layer thickness was determined. The 1-1/2- to 2-inch-thick natural boundary layers on the wind-tunnel side walls were artificially thickened by two methods. The first was a boundary-layer trip consisting of a series of adjustable-height fences transverse to the side-wall boundary-layer flow in the low subsonic region at the nozzle entrance. At subsonic Mach numbers this arrangement caused thickening by factors up to 3. However, the effectiveness of the trip as a thickening device fell off rapidly with increasing Mach number, and practically no thickening occurred at a Mach number of 2.5. The second method consisted of applying a distributed roughness coating that extended in 9-inch wide bands on each wall to various lengths down the nozzle. The roughness consisted of irregular-shaped grains (coarsely ground coffee beans having maximum dimensions ranging from 1/16 to about 1/8 inch) attached to the steel walls with a rubber-base adhesive. With the roughness bands extending to the viewing windows, the boundary layers at a Mach number of 2.5 were about 3-1/2 inches thick, as opposed to the natural thickness of 1-3/4 inches. However, at subsonic Mach numbers the distributed roughness was not so effective in increasing total thickness as the boundary-layer trips.

Some observations were made through separated boundary layers. With the M = 1.75 nozzle setting, driving the wind-tunnel terminal shock wave structure into the test section caused the boundary layer to separate. The shock was positioned by adjusting the back pressure in the diffuser so that the region of maximum separation (1/2 to 1 inch thick) was over the observing windows.

Although relative comparisons with the hot-wire anemometer indicated that the free-stream fluctuation level at all Mach numbers was at least an order of magnitude less than that in the boundary layers, there existed the possibility that the free-stream fluctuations could contribute measurably to the optical diffusion because, with thin boundary layers, the optical path through the free stream was up to four times as long as the path through the boundary layers themselves. This possibility was explored by employing a turbulence-promoting grid of bars at the nozzle entrance to increase the free-stream fluctuation level. Approximately doubling the free-stream fluctuation level as measured by the hot-wire anemometer had a negligible effect on the optical data at Mach numbers of 0.8 and 2.5.

A limited number of tests were conducted to determine the effect of air-stream humidity on the optical transmission characteristics. At supersonic Mach numbers, so long as the water vapor did not condense, little change in image quality could be detected. However, when condensate formed in the test section, the effect on the image was as if the source intensity had been decreased. This reduction of intensity due to water vapor, which amounted to as much as 20 percent, suggests that processes of skin cooling by liquid evaporation must be carefully controlled if liquids are injected upstream of receivers of visible radiation. Nominal test conditions at which the bulk of the data was obtained are given in table II. With few exceptions, any actual test condition corresponded to one of these nominal conditions with a relative error of less than ±3 percent.

Optical parameters.- To avoid the experimental difficulties associated with establishing a procedure for viewing through a single turbulent boundary layer, the two boundary layers on the wind-tunnel side walls were used as the basic configuration. It was felt that this experimental simplification was justified because equation (2) gives the possibility for reducing the results for two boundary layers to an equivalent result for one. Moreover, the validity of equation (2) is amenable to experimental verification by comparison of the results of observations through two boundary layers with the results of observations through four (eq. (3)). Thus, for each setting of Mach number, density level, and boundary-layer thickness, sets of optical data were taken for the two cases of single and double transmission of light beams through the test section.

A set of optical data consisted of the series of measurements of radiant flux which crossed the focal plane of the receiving telescope through each of the pinhole apertures listed in table I. The output

indication of the receiving photocell was directly proportional to the time-averaged value of the radiant energy which passed through each pinhole per unit time, and was related to the time-averaged value of the local intensity as follows:

$$P_F = E_F \frac{\pi D^2}{4} = \bar{I}_F \frac{\pi d^2}{4} = 2\pi \int_0^{d/2} I_F r \, dr \tag{14}$$

where d is the pinhole diameter, I_F is the time-averaged local intensity, considered a function of radius alone, and $\bar{I}_F$ is the average intensity over the aperture area.

To minimize the effects of molecular scattering, and imperfections in the optical components, and, further, to account for diffraction in the telephotometer, equation (14) was normalized with respect to conditions for no flow in the wind tunnel (test section at atmospheric pressure and temperature):

$$\frac{P_F}{P_{NF}} = \frac{E_F}{E_{NF}} = \frac{\bar{I}_F}{\bar{I}_{NF}} = \frac{\int_0^{d/2} I_F r \, dr}{\int_0^{d/2} I_{NF} r \, dr} \tag{15}$$

According to equation (15) when I_F is a different function of r than I_{NF}, the ratio E_F/E_{NF} becomes a function of the pinhole radius, $d/2$, and thus of the angular aperture θ_M, since

$$\theta_M = \tan^{-1} \frac{d}{2F} \doteq \frac{d}{2F} \tag{16}$$

where F is the focal length. As is shown in reference 6, equation (15) effectively eliminates the diffraction effects brought about by the finite entrance pupil of the telephotometer, and thus the quantity E_F/E_{NF} is a measure of the flux within a given solid angle due to boundary-layer effects alone, referred to the total flux per unit area, E_o, in the entering wave front; that is,

$$\left(\frac{E_F}{E_{NF}}\right)_n = \left(\frac{E_M}{E_o}\right)_n$$

Data to check equation (17) were obtained by varying the focal ratio of the telephotometer from f/8.6 to f/86. Decreasing the entrance pupil diameter from 2.5 inches to 0.25 inch increased the size of the diffraction image by factors up to 10. Tests with the largest focal ratio were inconclusive because the relatively small quantity of light available was spread over a large area of the focal plane, and difficulties were encountered in accurately centering the pinhole apertures. However, changes in focal ratio up to f/43 had no measurable effect on the ratio E_F/E_{NF} for given flow conditions.

Brief tests to assess the dispersion according to wave length in the scattered fields (Tyndall spectra) by capping the receiving telescope with filters were inconclusive because the spectral range covered by the available filters was small. It should be pointed out, however, that Baskins and Hamilton (ref. 6) report definite evidence of a spread in the scattered fields according to wave length, the shorter wave lengths being dispersed through larger angles.

Although the bulk of the data was obtained at normal incidence ($\varphi = 0$), limited tests were also carried out at an incidence angle of 45°. Because of inadequate clearances between the tunnel structure and the rearranged optical components, data could be obtained only for the case of double transmission.

Although the image of the point source was, typically, symmetric about the optical axis, a number of extraneous aerodynamic effects were encountered which had an undesirable influence on the image symmetry. If the incident beam intercepted a weak shock wave, the image acquired a tail oriented at the shock angle. Such situations were remedied by modification of the nozzle contours to eliminate the disturbance. During initial testing near a Mach number of 0.65, the image was observed to break up into a coarse-grating-type diffraction pattern. This behavior was traced to an acoustic grid of ultrasonic standing waves in the wind-tunnel test section excited by the boundary-layer rake. When the rake, which had a blunt trailing edge, was modified by addition of a sharp trailing edge, the image again became axisymmetric.

The fact that the test-section walls could not be maintained at room temperature for all test conditions gave rise to free-convective flows over the exteriors of the viewing windows. It is believed that in most cases this flow was laminar, but there was no convenient way to effect a calibration and it is conceivable that in certain instances free turbulence over the windows might have made a small contribution to the image deterioration. Accumulations of dirt on the windows were a continuing source of difficulty and annoyance. However, calibrations through clean and dirty windows established that runs of 4 to 6 hours duration introduced additional losses of less than 1 percent.

The optical parameters which were varied in combination with the various aerodynamic conditions are given in table III, and table IV is a tabulation of the aerodynamic and optical data for all configurations.

RESULTS AND DISCUSSION

Photometric Measurements

Effect of flow on transmitted power.- With the largest pinhole aperture (d = 0.033 in.) in the focal plane of the receiving telescope it was found that there was little difference in the radiant power received by the photocell for a condition of no flow in the wind tunnel and for the flow condition corresponding to the greatest image deterioration. In other words, the turbulent contributions to absorption, side- and back-scattering were not measurable with the present instrumentation, and the total energy in the incident wave for practical purposes always passed the entrance pupil of the telephotometer irrespective of the flow condition in the wind tunnel. This result, which was first reported by Baskins and Hamilton (ref. 6) can be interpreted to indicate (eq.(5)) that, in boundary layers having total thicknesses of the order of 1 inch, the integral scale of the density fluctuations is very much greater than the effective radiation wave length of 5200 angstrom units. Thus, in accordance with the theory of Booker and Gordon, it can be stated that the light field scattered by a compressible turbulent boundary layer is beamed principally in the forward direction. The maximum scattering angle encountered in the present tests has a value of 0.0006 radian, which corresponds to a condition of no loss through a pinhole aperture having a diameter of 0.025 inch.

Comparison of one- and two-transmission data.- In figure 3 the percentages of light reaching the phototube through various pinholes[4] for various flow conditions after penetrating two boundary layers are plotted against the corresponding percentages received after penetrating four. Only the data taken with the half-silvered mirror in place are shown. All these data, irrespective of flow condition or angular aperture, cluster with remarkably small scatter about a single curve. However, the mean line passing through the experimental data differs systematically from the theoretical prediction based on Lambert's law (eq. (3)). From equations (12) it is apparent that Lambert's law should apply for given angular aperture, because doubling the number of identical boundary layers penetrated by the light beam merely doubles the value of the fluctuation integral, thereby squaring the original intensity ratio as was shown previously (eq. (3)). Although part of the discrepancy between experiment and theory might be attributable to the fact that the paths of the incident and

[4]Because of negligible losses, the data for the two largest pinholes have been omitted from figure 3 and the following figures.

reflected light for the double-transmission cases did not coincide, the discrepancy is believed more probably to be caused by two secondary effects that are neglected in the theoretical treatment, namely, secondary scattering and scattering from rough interfaces between the boundary layers and the free stream. In the region where from 10 to 65 percent of the total energy is received through two boundary layers, a maximum increment of 0.04 in the value of $(E_F/E_{NF})_4$ over corresponding predictions based on Lambert's law occurs. This increment is believed due to reception of light which has been scattered more than once, that is, from solid angles outside that of the photometer. Further, in the region where from 65 to 100 percent is received, a maximum decrement between experiment and theory of 0.02 occurs. This decrement is attributed to a scattering of energy from the rough interfaces which occur between the boundary layers and the free stream (ref. 17). Due to interface scattering alone, the experimental data would be expected to lie below the theoretical curve throughout the range of intensity ratios and to be a function of the flow conditions. Secondary scattering, however, appears to act in a direction to counteract the decrement due to interface scattering and, moreover, to exert an influence which increases as the intensity ratio decreases. The net result of these two secondary effects is to cause the data of figure 3 to be independent of angular aperture and flow condition, but to depart systematically from the theoretical curve.

Because of these secondary effects, an apparent change in integral scale, l, will be observed, and the corresponding logarithms of the intensities at $\theta_M = 0$ will not, in general, be in the ratio of 2 to 1 for data corresponding to the single- and double-transmission cases. Thus after equation (13) is written for two and four boundary layers and θ_M is eliminated between them, an expression is obtained that contains the apparent integral scales and limiting intensities from the two measurements:

$$\left(\frac{E_M}{E_O}\right)_4 = \left(\frac{E_M}{E_O}\right)_2^{\left[\frac{1}{\frac{1+K_4}{1+K_2}\frac{\ln(E/E_O)_2}{\ln(E/E_O)_4} - \frac{1}{\ln(E/E_O)_4}\left(\frac{1+K_4}{1+K_2} - 1\right)\ln\left(\frac{E_M}{E_O}\right)_2}\right]} \tag{18}$$

where

$$\ln\left(\frac{E}{E_O}\right)_n = -\frac{2\pi^2 l_n}{\lambda^2}\int_0^{n\delta}\overline{\left(\frac{\Delta\epsilon}{\epsilon}\right)^2}\,dy$$

The empirical curve defined by the data in figure 3 is given by:

$$\left(\frac{E_M}{E_O}\right)_4 = \left(\frac{E_M}{E_O}\right)_2^{\left[\frac{1}{0.44-0.14\ \ln(E_M/E_O)_2}\right]} \quad \text{for} \quad \left(\frac{E_M}{E_O}\right)_2 \geq 0.10$$

Therefore, the data indicate the following empirical result

$$0.44 = \left(\frac{1 + K_4}{1 + K_2}\right) \frac{\ln(E/E_O)_2}{\ln(E/E_O)_4}$$

$$0.14 = \frac{1}{\ln(E/E_O)_4} \left(\frac{1 + K_4}{1 + K_2} - 1\right)$$

Consequently, the integral scale and intensity of turbulent density fluctuations for two boundary layers can be obtained in terms of the corresponding quantities for four boundary layers for this series of experiments by use of the following empirical expressions (for $(E_M/E_O)_2 \geq 0.10$):

$$\left.\begin{aligned} \ln\left(\frac{E}{E_O}\right)_2 &= \frac{0.44\ \ln(E/E_O)_4}{1 + 0.14\ \ln(E/E_O)_4} \\ 1 + \left(\frac{4\pi l_2}{\lambda}\right)^2 &= \frac{1 + (4\pi l_4/\lambda)^2}{1 + 0.14\ \ln(E/E_O)_4} \end{aligned}\right\} \qquad (19)$$

It is reasonable to expect that for the same intensity ratios, a comparison between one boundary layer and two boundary layers would yield smaller departures from Lambert's law than is shown in figure 3 for the case of two and four because the number of boundary-layer interfaces is cut in half and because opportunity for the occurrence of secondary scattering decreases. The dash-dot curve lying halfway between the experimental curve and the prediction based on Lambert's law, which is shown in figure 3, is an estimate of the relation expected to hold between one boundary layer and two. This curve is subsequently used to reduce the optical data to results applicable to an equivalent single boundary layer. The empirical equation for this curve is:

$$\left(\frac{E_M}{E_O}\right)_2 = \left(\frac{E_M}{E_O}\right)_1^{\left[\frac{1}{0.48-0.08\ \ln(E_M/E_O)_1}\right]} \quad \text{for} \quad \left(\frac{E_M}{E_O}\right)_1 \geq 0.28 \tag{20}$$

Comparison of data with scattering theory.- Figure 4 has been prepared to compare the results of the theoretical scattering analysis with the test results for compressible turbulent boundary layers. The theory based on the two-parameter turbulence model of Booker and Gordon predicts the straight-line functional dependence given by equation (13) and depicted in sketch (a). Figure 4(a) presents single-transmission data at a Mach number of 2.00 and a density ratio of 0.46 for each of boundary-layer configurations (1) through (4) (table II) plotted in the coordinate system suggested by the analysis. In each case the straight-line dependence predicted by theory is obtained, and thus the turbulent density fluctuations can be defined in terms of the two parameters given by the extrapolated intercepts with the axes.

That wide changes in Mach number and density ratio have little effect on this functional behavior is further illustrated in figure 4(b), which is a normalized form of figure 4(a). The ordinate of figure 4(b) is the left-hand side, and the abscissa is the right-hand side of the following rearranged form of equation (13):

$$\frac{1}{\ln(E_M/E_O)_2} - \frac{1}{\ln(E/E_O)_2} = \frac{1+(4\pi l_2/\lambda)^2}{\ln(E/E_O)_2} \tan^2\frac{\theta_M}{2}$$

Optical data corresponding to a given flow condition were plotted as indicated in figure 4(a) and fitted with a straight line. The x and y axis intercepts determine the constants $\ln(E/E_O)_2$ and $\frac{1+(4\pi l_2/\lambda)^2}{\ln(E/E_O)_2}$. Graphical curve fitting was used for most cases; but where the scatter was considered excessive, the constants were determined by the method of least squares. Fitting the straight line was accomplished by the method of weighting of functions described in reference 22. In the present case this weighting procedure had the effect of decreasing the weight of those data corresponding to intensity ratios which were both larger and smaller than a value of $1/e$ (=0.368).

Notwithstanding the considerable variation of Mach number, free-stream density, and boundary-layer thickness represented by the various symbols shown in figure 4, it can be observed that departures from linearity are small. It therefore appears that the fluctuating density fields

in compressible turbulent boundary layers behave as though they were isotropic insofar as the transmission of light is concerned. Consequently, photometric measurements in the radiation field produced by the interaction of a plane light wave with a turbulent boundary layer can be used in conjunction with scattering theory to deduce average values of the integral scale and the intensity of turbulent density fluctuations.

Effect of Turbulent Density Fluctuations on Optical Images

It has been shown so far that the scattering analysis based on the cross section of Booker and Gordon is in good functional agreement with experiment, and, further, that the turbulence structure can be defined by two parameters deduced from the data. With this information, one can compute for a given flow the distribution of radiant intensity at the focal plane of a diffracting optical imaging device. To carry out this calculation, one equates equations (12) and (15) by using equation (17), and changes variables as follows:

$$\tan^2 \frac{\theta_M}{2} \doteq \left(\frac{r}{2F}\right)^2$$

$$r = \left(\frac{F\bar{\lambda}}{\pi D}\right) \xi$$

After differentiating the resulting expression with respect to the dimensionless radius ξ and simplifying, one obtains

$$I_F = e^{\frac{\ln E/E_O}{1+(1+K)(\bar{\lambda}/2\pi D)^2\xi^2}} \left\{ I_{NF} - \frac{2(1+K)\ln E/E_O}{\left[1+(1+K)(\bar{\lambda}/2\pi D)^2\xi^2\right]^2} \int_O^\xi I_{NF}\xi \, d\xi \right\}$$

For an axially symmetric objective one has for I_{NF} the well-known result of Airy:

$$\frac{I_{NF}}{I_{NF}\Big|_{\xi=0}} = \left[\frac{2J_1(\xi)}{\xi}\right]^2$$

where $J_1(\xi)$ is the Bessel function of unit order. It therefore follows that the intensity at a point ξ in the focal plane due to turbulence relative to that on the optical axis without turbulence is:

$$\frac{I_F}{I_{NF}\Big|_{\xi=0}} = e^{\frac{\ln E/E_0}{1+(1+K)(\bar{\lambda}/2\pi D)^2\xi^2}} \left\{ \left[\frac{2J_1(\xi)}{\xi}\right]^2 - \frac{2(1+K)\ln E/E_0}{\left[1+(1+K)(\bar{\lambda}/2\pi D)^2\xi^2\right]^2} \int_0^{\xi} \frac{[2J_1(\xi)]^2}{\xi} d\xi \right\} \tag{21}$$

Graphs of equation (21) for the no-flow condition and for three typical flow conditions with boundary-layer configuration (3) are compared in figure 5 with each other and also with corresponding photomicrographs of the single-transmission image at the focal plane of the receiving telescope. For each graph, the two parameters involving the turbulence structure were evaluated from single-transmission photometric measurements in the manner previously described, and the two optical constants, $\bar{\lambda}$ and D, were assigned the values appropriate to the instrumentation used in the present tests. The effect of center-blocking is small and can be safely neglected.

The ordinates at the point $\xi = 0$ in each of the four graphs in figure 5 have been given the same physical height. However, the relative numerical values of the peaks are actually shown to be in the ratios 1:0.5:0.2:0.1 as one proceeds down the column. An intensity ratio of unity on the optical axis corresponds to the no-flow condition shown by the graph and the photographs along the top row. Each of the graphs of the intensity ratios for the three flow conditions also shows as an additional dashed curve an attenuated no-flow distribution. This dashed curve arises from the first term on the right-hand side of equation (21) and can be interpreted as the portion of the intensity distribution composed of unscattered radiation. Note on the graphs that as the value of the central maximum decreases with increasing air density, the height of the total intensity distribution curve relative to the corresponding no-flow curve increases and that the dark rings of the diffraction pattern (ξ = 3.8, 7.0, 10.1, . . .) disappear. This indicates that increasing fractions of radiant energy are scattered outside the Airy disc. For example, the ratio of the flow and no-flow ordinates at the maximum of the second bright ring ($\xi \doteq 8.6$) are 7/1, 22/1, and 32/1, respectively, for the 0.157, 0.295, and 0.379 density ratios.

The photomicrographs of the images to the right of each plot in figure 5 are visual evidence of the increased scatter that occurred as the density was increased at a Mach number of 2. Unfortunately, due to halation in the film and limitations in the reproduction process, the

photographic images show considerably less detail than can be observed visually, or for that matter, on the original negatives. The Airy disc, the first two bright rings, and portions of the third bright ring can be readily distinguished on the negatives for the case of no flow. The extraneous spots of light visible on some of the photographs are "ghosts" originating from second-surface reflections, and they represent less than 1 percent of the total flux. The exposure times (15, 45, and 90 seconds) for the three columns of images shown were selected so that points of equal brightness on the film in any row were exposed by light intensities in the ratio 6:2:1. With flow at a Mach number of 2 (bottom three rows of pictures), the intensity of the central disc is noticeably attenuated (15-second column) and the zone of the focal plane outside the disc becomes illuminated correspondingly (45- and 90-second columns). Except for the small influence of secondary scattering, these qualitative effects of the scatter and redistribution have been predicted by the previous analysis.

A further feature of the photographs for the flow conditions shown in figure 5 should be mentioned. The maximum intensity ratios calculated as belonging to each row and the selected exposure times for each column of photographs cause adjacent pictures on a diagonal (dhl, for example) to exhibit approximately the same response; for by the reciprocity law for photographic emulsions, the increased exposure times along the diagonal serve to counteract the decrease in light intensity caused by the additional scattering that occurred. Therefore, increases of the diameter of the image along the diagonal dhl illustrate that even though one can compensate for the attenuation due to turbulence by increasing the gain of the system (that is, increasing exposure time here or increasing the amplification factor of a photomultiplier circuit) a loss in resolution will be inevitable.

Dependence of Optical Transmission Characteristics on Mean Flow Conditions

Establishment of correlating parameter.- There has been no attempt so far to connect the scattering of radiant energy with the dynamics of the mean boundary-layer flow because it is clear from the preceding discussion that Mach number, density level, and boundary-layer thickness are important only insofar as they contribute to the formation of density "lumps." For reasons of practical utility, however, it would be desirable to utilize some average characteristic of the mean boundary-layer flow as a measure of the turbulence pattern controlling the scattering of light. Unfortunately, the lack of knowledge concerning the relationship between the turbulence structure and the mean flow in a compressible turbulent boundary layer prohibits the formulation on any other than an empirical basis.

As a preliminary to the formulation of such a parameter, it is noted that, when plotted as shown in sketch (a) and figure 4(a), the photometric data exhibit the following characteristics:

1. Increases of Mach number, density, and boundary-layer thickness produce substantial decreases in the slopes of the straight lines passed through the data.

2. Relatively large changes in Mach number, density, and boundary-layer thickness produce comparatively small changes in the absolute values of the extrapolated intercepts with the abscissa, and, moreover, the intercepts in most cases have small numerical values as compared to the numerical values of the aperture function $\tan^2(\theta_M/2)$.

In other words, displacements of the present data regarded as shifts in the coordinate axes are much less extensive than displacements regarded as rotations of the coordinate axes. Thus the slopes of the lines alone will serve as a good over-all measure of the effects of Mach number, density, and boundary-layer thickness on the scattering process, and one can, with little loss in accuracy, consider that the straight lines passed through the data also pass through the origin of the coordinate system. The mathematical conditions to be met for this simplification to be valid are:

$$0 \approx \frac{1}{1 + K} \doteq \left(\frac{\lambda}{4\pi l}\right)^2 << \left(\frac{\theta_M}{2}\right)^2 \doteq \tan^2 \frac{\theta_M}{2}$$

or

$$(1 + K)\left(\frac{\theta_M}{2}\right)^2 \doteq K\left(\frac{\theta_M}{2}\right)^2 >> 1$$

In the present tests these limitations are fulfilled for all of the pinhole apertures for some of the test conditions, and for most of the larger pinhole apertures for all test conditions. Equation (12) can therefore be written in the following form independent of explicit dependence on the radiation wave length:

$$\ln \frac{E_M}{E_o} \doteq - \frac{1}{2l\theta_M{}^2} \int_o^{\delta} \overline{\left(\frac{\Delta\epsilon}{\epsilon}\right)^2}\, dy \qquad (22)$$

Thus, a parameter based on mean flow conditions which is proportional to the right-hand side of equation (22) can be expected to effect a correlation of the intensity ratio data, at least for the larger pinhole

apertures. It should be noted that the flow-dependent portion of the exponent of equation (22) can be cast into a form which bears a very close resemblance to the corresponding expression obtained by Liepmann (ref. 2) for the mean square deviation of a ray. If one rewrites equation (22) as follows

$$- \theta_M^2 \ln\left(\frac{E_M}{E_O}\right) = \frac{1}{2l} \int_O^\delta \overline{\left(\frac{\Delta\epsilon}{\epsilon}\right)^2} dy$$

and notes that the left-hand side must be constant for a given flow condition, it is obvious that each set of optical data can be described by a single number, say the mean square deviation of a ray, $\overline{\theta^2}$. If, further, the integral on the right-hand side of the above expression is written as the product of an average value of the integrand and the boundary-layer thickness, one obtains

$$\overline{\theta^2} \sim - \theta_M^2 \ln\left(\frac{E_M}{E_O}\right) = \frac{\delta}{2l} \overline{\left(\frac{\Delta\epsilon}{\epsilon}\right)^2}_{av} \tag{23}$$

This relation corresponds functionally to equation III-2 of reference 2. Liepmann approximated equation (23) in terms of the mean flow variables by: (1) setting the root mean square density fluctuation proportional to the over-all change in mean density across the boundary layer, (2) setting the scale of the fluctuations proportional to the thickness of the laminar sublayer, and (3) setting the total boundary-layer thickness proportional to the length of boundary-layer run divided by the 1/5 power of the length Reynolds number. This approach leads to the following result for the root mean square deviation of a ray:

$$\sqrt{\overline{\theta^2}} \sim (\rho_\infty)\left[\frac{(\gamma-1)M_\infty^2/2}{1+(\gamma-1)M_\infty^2/2}\right]\left(\begin{matrix}\text{length} \\ \text{Reynolds no.}\end{matrix}\right)^{2/5}\left(\begin{matrix}\text{local skin-friction} \\ \text{coefficient}\end{matrix}\right)^{1/4}$$

For any one of the boundary-layer configurations listed in table II the optical data from the present experiments can be correlated by a parameter proportional only to the first two factors in the foregoing expression, that is, the free-stream density and free-stream Mach number function. However, attempts to incorporate into the parameter the relatively weak effects of the various boundary-layer thicknesses and profile shapes (Reynolds number and skin-friction coefficient) by the use of functions of displacement, momentum, or energy-loss thickness were not an unqualified success. These correlations usually led to a spread of the

unseparated-flow data as a function of Mach number and did not correlate the separated boundary-layer data at all.

The inadequacy of that portion of Liepmann's parameter proportional to the ratio of boundary-layer thickness and turbulence scale is believed due to the use in equation (23) of flow parameters proportional to the microscale of the turbulence. The present analysis, however, identifies the length, l, in equation (23) as the integral scale of the fluctuations rather than as the microscale. According to references 16, 17, and 18, the flow parameter proportional to the integral scale is the total boundary-layer thickness, δ. Hence the right-hand side of equation (23) is actually insensitive to boundary-layer thickness except as it influences the local intensity of the density fluctuations and thus the average. This latter effect can be taken into account by a slight generalization of that portion of Liepmann's parameter which includes the fluctuation contributions. Instead of setting the fluctuations proportional to the over-all difference between the density at the wall and in the free stream as Liepmann has done, it has been found advantageous to employ the integral across the layer of the difference between the free-stream density and the local density within the layer. Thus, defining the boundary-layer parameter:

$$\beta' = \int_0^{\delta} (\rho_\infty - \rho)\,dy \tag{24}$$

and introducing the usual flat-plate assumptions that the total temperature and static pressure do not vary across the boundary layer, one finds that

$$\beta' = \rho_\infty \left[\frac{(\gamma - 1)M_\infty^2/2}{1 + (\gamma - 1)M_\infty^2/2}\right] \int_0^{\delta} \left[1 - \left(\frac{M}{M_\infty}\right)^2\right] dy$$

This relation is rendered dimensionless by introducing the standard sea-level density, $\bar{\rho}$, and the effective radiation wave length, $\bar{\lambda}$, so that

$$\beta = \frac{\beta'}{\bar{\rho}\bar{\lambda}} = \frac{\rho_\infty}{\bar{\rho}\bar{\lambda}} \left[\frac{(\gamma - 1)M_\infty^2/2}{1 + (\gamma - 1)M_\infty^2/2}\right] \int_0^{\delta} \left[1 - \left(\frac{M}{M_\infty}\right)^2\right] dy \tag{25}$$

With respect to the free-stream density and free-stream Mach number dependences, the parameter β (eq. (24)) is identical to the analogous expression given by Liepmann in reference 2. However, whereas Liepmann's parameter incorporates the ratio of the total boundary-layer thickness

to turbulence scale in terms of Reynolds number and skin-friction coefficient, the parameter β utilizes a thickness weighted with respect to the Mach number profile. No general significance can be attached to the parameter β, and its use can be justified only on the practical ground that it is more effective in correlating the data than the other arrangements which were tried.

Samples of the boundary-layer Mach number profiles typical of those used to calculate the parameter β are shown in figure 6, for a free-stream density of 0.23 standard sea-level atmospheres. The small differences between boundary-layer Mach numbers at corresponding y distances on opposite walls of the wind tunnel were averaged arithmetically. Distances through the boundary layer are normalized with respect to the energy-loss thickness, which is defined in the figure. A sample of the Mach number profile for the case of the separated boundary layer (configuration (5)) is also shown. It can be seen from the figure that the shape of the separated layer is significantly different from the others. It will appear shortly that this difference had an effect on the optical transmission characteristics which was adequately accounted for by the parameter β.

Correlation of optical data with aerodynamic conditions.- Figure 7 shows the fraction of energy remaining in the light beam after traversing four and two boundary layers as a function of the flow and optical variables combined into the parameter $\beta/\theta_M \cos\varphi$. The limits for one boundary layer were estimated by the use of figure 3. The correlation parameter incorporates the factor $\cos\varphi$ so that data obtained at the angle of incidence of 45° could be included in the figure.

Notwithstanding the wide range of Mach numbers, density levels, boundary-layer shapes and thicknesses represented by the symbols defining the family of curves in figure 7, and irrespective of the small departures from insulated wall conditions due to heat transfer, the parameter $\beta/\theta_M \cos\varphi$ effects an adequate correlation of all the data. The fact that this parameter correlates the data as shown implies that

$$\beta^2 \sim \frac{1}{l}\int_0^{\delta} \overline{\left(\frac{\Delta\epsilon}{\epsilon}\right)^2}\, dy$$

This proportionality follows from the two observations that the data in figure 7 can be empirically represented by an equation of the form $\ln E_M/E_O \sim -(\beta/\theta_M \cos\varphi)^2$ and that equation (22) gives the corresponding analytic prediction. Thus these data serve to provide an approximate over-all relationship between the turbulence structure and the mean flow conditions in the boundary layers.

Some of the data shown in figure 7 which are associated with the smaller pinhole apertures show a tendency to break off from the main group at various positions along the descending portion of the band. Curves for a typical optical set (filled symbols) are shown illustrating this tendency. The dashed portions of the curves correspond to a linear extrapolation of the data; in figure 4(a) this region of extrapolation corresponds to the distance between the y intercept and the first data point. This behavior is in accord with the analytic predictions, which indicate that for constant turbulence structure, that is, constant β, a decrease of the angular aperture to zero causes the intensity ratio to approach a finite lower limit (fig. 4(a)). The exact manner in which the curve would approach the asymptote, however, is a function of the integral scale of the turbulence, and thus of the given flow condition.

It is apparent from examination of figure 7 that the moderately thick turbulent boundary layers explored in the present investigation, even at high subsonic Mach numbers, have an important influence on the propagation of light, the influence being to scatter increasing fractions of the originally collimated beam as the Mach number, density, and boundary-layer thickness increase. In fact, the estimated curves for one boundary layer indicate that when $\beta/\theta_M \cos\varphi$ is about 5×10^8, an attenuation of the incident wave to a value of $E_M/E_o = 1/e$ ($= 0.368$) can be expected. In contrast, the same attenuation in the sea-level atmosphere due to molecular scattering alone would require propagation over a distance of about 75 miles.

Effect of scattered light on optical resolution.- Although the turbulence-scattered light is deviated through very small angles, the deleterious effect on an optical imaging device can be large because scattered light from a given point in the object goes into a finite area in the image. The effect can be conveniently evaluated by establishing a resolution criterion analogous to the Rayleigh limit of resolution due to diffraction.

The Rayleigh resolution limit (ref. 7) can be expressed as the angle subtended between two equally bright point objects whose images overlap in the back focal plane of an optical imaging instrument by an amount just equal to the radius of the Airy disc of either image. Roughly 85 percent of the energy radiated into the entrance pupil by each point object is found in each disc; and the intensity distributions and disc radii are fixed by the focal ratio of the instrument and the wave length of the radiation. The angle subtended at the objective of an axially symmetric instrument by the Airy disc radius is (for $D >> \lambda$):

$$\theta_R \doteq \frac{1.22\lambda}{D} \tag{26}$$

On the other hand, light which has passed through a turbulent boundary layer has been seen to appear at the focal plane in a much larger disc (fig. 5), with energy distribution determined primarily by the intensity and scale of the boundary-layer density fluctuations. In analogy to the Rayleigh criterion, one can propose that the radius of the disc containing 85 percent of the total energy establishes the resolution limit due to turbulence. Thus, one accepts as tolerable a 15-percent loss, which serves to identify in figure 7 a minimum value of $\beta/\theta_M \cos\varphi$ of about 10^8 for a single boundary layer. The ratio of the boundary-layer resolution limit for any value of β and the Rayleigh resolution limit due to diffraction for an axially symmetric imaging device then can be expressed as

$$\frac{\theta_B}{\theta_R} = \frac{\beta D}{1.22\lambda \cos\varphi} \times 10^{-8} \qquad (27)$$

The interpretation of equation (27) is best illustrated by an example. The resolution limit of the 2.5-inch-diameter objective used in the present experiments is about 2 seconds of arc; that is, $1.22\lambda/D$ is about 1×10^{-5} radian for $\bar{\lambda}$ = 5200 angstroms. With β = 3900, the ratio of the resolution limit due to turbulence to the resolution limit due to diffraction takes a value of 3.9. This value of β happens to correspond to a 1-3/4-inch-thick turbulent boundary layer at a Mach number of 2.5 and a density altitude of about 45,000 feet (table IV). It should be noted that according to equation (27) an objective of large diameter will be more severely affected than will one of moderate size. Optical imaging equipment such as sextants, cameras, and fire control sights will be similarly affected.

CONCLUSIONS

The results of tests to determine the optical transmission characteristics of turbulent boundary layers on an effectively insulated flat plate over ranges of Mach number from 0.4 to 2.5, free-stream density from 0.12 to 0.93 standard sea-level atmospheres, and boundary-layer thickness from 1-1/2 to 4-1/2 inches lead to the following conclusions:

1. The loss in radiant intensity from a collimated beam of unpolarized white light after penetrating a turbulent boundary layer depends mainly upon the integral scale and intensity of the density fluctuations. This result is in agreement with a theoretical prediction based on the scattering cross section of Booker and Gordon. A parameter proportional

to the space integral of the cumulative change in mean density across the boundary layer is found to provide an over-all measure of the intensity loss over the range of flow parameters investigated.

2. The scattered light is deviated in all cases through small angles, the maximum deviation from the direction of primary propagation being about 0.0006 radian in the present tests; and the angular distribution of scattered energy depends upon the integral scale of the density fluctuations. This result also agrees with the scattering theory based on the scattering cross section of Booker and Gordon.

3. Comparison of the transmission characteristics of two boundary layers with those of four boundary layers indicates small deviations from Lambert's law of exponential attenuation which probably result from secondary scattering and diffuse refraction from the boundary-layer free-stream interfaces.

4. Due to the foregoing effects, significant losses in resolving power can be sustained by optical imaging devices which receive energy through compressible turbulent boundary layers. For example, a 1-3/4-inch-thick turbulent boundary layer at a Mach number of 2.5 and a density altitude of 45,000 feet introduces a loss of resolving power greater by a factor of 3.9 than the Rayleigh resolution limit for a 2-1/2-inch objective.

5. Photometric measurements in the radiation field produced by the interaction of a turbulent boundary layer with a plane light wave can be used in conjunction with electromagnetic theory to deduce average values of the integral scale and the intensity of the turbulent density fluctuations. Provided that the limitations of the Booker and Gordon analysis are not exceeded, this conclusion is believed to be valid also for turbulent flows other than boundary layers and for radiations at wave lengths outside the visible range.

Ames Aeronautical Laboratory
National Advisory Committee for Aeronautics
Moffett Field, Calif., Feb. 21, 1956

REFERENCES

1. Seiff, Alvin: A Free-Flight Wind Tunnel for Testing at Hypersonic Speeds. NACA Rep. 1222, 1954.

2. Liepmann, H. W.: Deflection and Diffusion of a Light Ray Passing Through a Boundary Layer. Rep. SM-14397, Douglas Aircraft Co., May 16, 1952.

3. Booker, H. G., and Gordon, W. E.: A Theory of Radio Scattering in the Troposphere. Proc. of the I.R.E., vol. 38, no. 4, Apr. 1950, pp. 401-412.

4. Villars, F., and Weisskopf, V. F.: The Scattering of Electromagnetic Waves by Turbulent Atmospheric Fluctuations. Physical Review, vol. 94, no. 2, Apr. 15, 1954, pp. 232-240.

5. Baskins, L. L., and Hamilton, L. E.: Preliminary Wind Tunnel Investigation on the Optical Transmission Characteristics of a Supersonic Turbulent Boundary Layer. Rep. G.M.-1.27, Northrop Aircraft, Apr. 1952.

6. Baskins, L. L., and Hamilton, L. E.: The Effect of Boundary Layer Thickness Upon the Optical Transmission Characteristics of a Supersonic Turbulent Boundary Layer. Rep. NAI-54-756, Northrop Aircraft, Nov. 11, 1954.

7. Jenkins, Francis A., and White, Harvey E.: Fundamentals of Physical Optics. McGraw-Hill Book Co., 1937.

8. Houstoun, R. A.: A Treatise on Light. Seventh Ed., Longmans, Green and Co., Ltd., 1938.

9. Bhagavantum, S.: Scattering of Light and the Raman Effect. Chem. Pub. Co., 1942.

10. Wheelon, A. D.: Note on Scatter Propagation with a Modified Exponential Correlation. Proc. of the I.R.E., vol. 43, no. 10, Oct. 1955, pp. 1381-1383.

11. Muchmore, R. B., and Wheelon, A. D.: Line of Sight Propagation Phenomena - I. Ray Treatment. Proc. of the I.R.E., vol. 43, no. 10, Oct. 1955, pp. 1437-1449.
Wheelon, A. D., and Muchmore, R. B.: Line of Sight Propagation Phenomena - II. Scattered Components. Proc. of the I.R.E., vol. 43, no. 10, Oct. 1955, pp. 1450-1458.

12. Staras, Harold: Forward Scattering of Radio Waves by Anisotropic Turbulence. Proc. of the I.R.E., vol. 43, no. 10, Oct. 1955, pp. 1374-1380.

13. Richtmyer, F. K., and Kennard, E. H.: Introduction to Modern Physics. Third Ed., McGraw-Hill Book Co., 1942, pp. 478, 479.

14. Tabibian, Richard M.: Particle Size Determination of Spherical Colloidal Particles by Light Scattering. (I) - The Specific Turbidity. Tech. Rep. No. 10, Wayne Univ., Aug. 20, 1954.

15. Middleton, W. E. Knowles: The Effect of the Angular Aperture of a Telephotometer on the Telephotometry of Collimated and Non-Collimated Beams. Jour. Optical Soc. of Amer., vol. 39, no. 7, July 1949, pp. 576-581.

16. Klebanoff, P. S., and Diehl, Z. W.: Some Features of Artificially Thickened Fully Developed Turbulent Boundary Layers With Zero Pressure Gradient. NACA TN 2475, 1951.

17. Klebanoff, P. S.: Characteristics of Turbulence in a Boundary Layer With Zero Pressure Gradient. NACA TN 3178, 1954.

18. Schubauer, G. B., and Klebanoff, P. S.: Investigation of Separation of the Turbulent Boundary Layer. NACA TN 2133, 1950.

19. Hopkins, H. H.: The Concept of Partial Coherence in Optics. Proc. Roy. Soc. of London, series A, no. 1093, vol. 208, Aug. 22, 1951, pp. 263-277.

20. Gabor, D.: Microscopy by Reconstructed Wave-Fronts. Proc. Roy. Soc. of London, series A, no. 1051, vol. 197, July 7, 1949, pp. 454-487.

21. Rogers, G. L.: The Abbé Theory of Microscopic Vision and the Gibbs Phenomenon. Amer. Jour. Phys., vol. 22, no. 6, Sept. 1954, pp. 384-389.

22. Scarborough, James B.: Numerical Mathematical Analysis. The Johns Hopkins Press, 1930., pp. 370-374.

TABLE I.- RANGE OF ANGULAR APERTURES OF TELEPHOTOMETER

Pinhole	Diameter, $d \times 10^3$, in.	Nominal angular aperture, $\theta_M \times 10^5$, radian	Plotting symbol
1a, 1b	0.75, 0.71	1.70	○
2a, 2b	1.01, 1.07	2.43	□
3a, 3b	1.28, 1.23	2.91	◇
4a, 4b	1.80, 1.85	4.24	△
5a, 5b	3.32, 3.27	7.70	▽
6a, 6b	4.20, 4.07	9.63	▷
7a, 7b	4.86, 4.71	11.13	⬠
8a, 8b	8.09, 8.14	18.92	⬡
9	15.4	35.9	
10	33.0	76.9	

TABLE II.- RANGE OF AERODYNAMIC VARIABLES

Mach no. designation M_∞, Nominal			I 0.40	II 0.67	III 0.80	IV 1.30	V 1.40	VI 1.75	VII 2.00	VIII 2.50
Density ratio	$\frac{\rho_\infty}{\bar{\rho}}$	Plotting symbol	◇ (a)	▷ (a)	▷ (a)	▽ (a)	▷ (a)	◇ (a)	□ (a)	○ (a)
A	0.116	—○	---	---	---	---	①,②	①-④	①-④	①-④
B	.232	○	②,③	①-③	①-④	⑤,⑥	①-④	①-④	①-④	①-④
C	.463	○	②,③	①-④	①-④	⑤,⑥	①-④	①-④	①-④	---
E	.694	○	①-③	①-④	①-④	---	---	---	---	---
F	.925	○—	①-④	①-④	①-④	---	---	---	---	---

[a]Flow configuration:

① Tunnel clean △

② Boundary-layer trip at nozzle entrance △

③ Rough side walls to within 40 inches of observing window △

④ Rough side walls to within 10 inches of observing window △

⑤ ① + shock-induced separation ▽

⑥ ③ + shock-induced separation ▽

TABLE III.- RANGE OF OPTICAL VARIABLES

Angle of incidence φ, deg	No. of transmissions, n/2	Focal ratio f/no.	Filter designation Wratten no.	Angular apertures,[a] θ_M (table I)	Aerodynamic variables, table II		
					Boundary-layer configuration	Mach no.	Density ratio
0	1, 2	8.6	None	1-10	①-④	V-VIII	A
0	1, 2	8.6	None		①-④	III, V-VIII	B
0	1, 2	8.6	None		①-④	II,III,V,VI, VII	C
0	1, 2	8.6	None		①-④	II,III	E
0	1, 2	8.6	None		①-④	I-III	F
[b]45	2	8.6	None		④	III,V	B, C
[b]45	2	8.6	None		③	III,V	B, C
0	1, 2	12.3	None		①,③	VIII	B
0	1, 2	17.2	None		①,③	VIII	B
0	1, 2	[c]28.6	None		③	III	F
0	1, 2	[d]42.9	None		③	III	F
0	2	[e]85.8	None		③	VII	C
0	2	8.6	45		③	III	F
0	2	8.6	61		②	III	F

[a]Series "b" apertures used for configuration ③ only

[b]Special plotting symbol for $\varphi = 45^\circ$: III - C: ◈
V - C: ◇

[c]Entrance pupil covered by opaque mask with 3/4-inch-diameter hole centered 3/4 inch off optical axis

[d]Entrance pupil covered by opaque mask with 1/2-inch-diameter hole centered 1/2 inch off optical axis

[e]Entrance pupil covered by opaque mask with 1/4-inch-diameter hole centered 1/4 inch off optical axis

TABLE IV.- TABULATION OF DATA

M	$\frac{\rho_\infty}{\bar{\rho}}$	β	δ, ft	$\frac{n}{2}$	E_M/E_o for aperture diameters, dx10³ inch							
					8.09	4.86	4.20	3.32	1.80	1.28	1.01	0.75
(a) Boundary-layer configuration (1); φ = 0°, D = 2.5 in.												
0.40	0.928	458	0.09	2	1.00	1.00	1.00	1.00	1.00	0.992	0.943	0.920
.69	.228	316	.12	1	1.00	1.00	.995	1.00	1.00	.991	.984	.968
.68	.457	583	.12	1	1.00	.997	.994	1.00	.980	.981	.961	.933
.69	.680	913	.11	1	.999	.999	.999	1.00	.989	.954	.906	.874
.66	.922	1110	.11	1	.996	.992	.991	.981	.953	.902	.836	.763
.69	.228	316	.12	2	1.00	.994	1.00	.995	.990	.962	.952	.945
.68	.457	583	.12	2	.999	.993	1.00	.990	.964	.928	.897	.864
.69	.680	913	.11	2	.994	.986	.990	.982	.919	.837	.755	.686
.66	.922	1110	.11	2	.990	.976	.980	.961	.875	.769	.673	.592
.82	.228	412	.11	1	1.00	1.00	1.00	.996	.995	.984	.976	.973
.82	.456	824	.12	1	.999	.999	1.00	.994	.981	.947	.907	.855
.81	.693	1160	.11	1	.996	.990	.986	.982	---	.870	.807	.731
.81	.920	1530	.11	1	.989	.981	.968	.950	.861	.761	.672	.578
.82	.228	412	.11	2	1.00	.996	1.00	.996	.980	.960	.931	.925
.82	.456	824	.12	2	.995	.985	.990	.975	.921	.862	.786	.709
.81	.693	1160	.11	2	.986	.971	.965	.933	.818	.710	.599	.503
.81	.920	1530	.11	2	.976	.941	.927	.888	.685	.540	.421	.330
1.43	.112	928	.15	1	1.00	.997	.997	.998	.985	.974	.946	.931
1.43	.226	1740	.15	1	.998	.994	.998	.987	.960	.936	.884	.838
1.42	.452	3100	.17	1	.988	.969	.962	.965	.865	.753	.625	.535
1.44	.116	928	.15	2	.999	.999	1.00	.995	.985	.965	.910	.890
1.43	.221	1730	.15	2	.994	.987	.989	.972	.927	.853	.762	.671
1.42	.452	3150	.17	2	.976	.951	.952	.903	.733	.557	.418	.336
1.78	.118	1380	.16	1	1.00	1.00	1.00	.995	.980	.964	.941	.935
1.78	.224	2270	.18	1	.996	.988	.986	.976	.949	.895	.837	.762
1.77	.444	3960	.16	1	.982	.957	.949	.933	.780	.639	.520	.416
1.75	.115	1140	.16	2	.997	.987	.989	.976	.957	.917	.872	.790
1.76	.227	2260	.18	2	.989	.969	.968	.952	.869	.764	.661	.569
1.76	.448	4230	.16	2	.963	.914	.892	.833	.595	.417	.306	.218
1.98	.112	1370	.15	1	.998	.996	.992	.971	.968	.934	.909	.877
2.00	.232	2700	.14	1	.991	.981	.974	.962	.886	.803	.712	.613
2.00	.463	4760	.14	1	.972	.931	.908	.860	.656	.498	.378	.287
2.04	.116	1410	.15	2	.984	.966	.961	.929	.801	.667	.528	.460
2.00	.230	2570	.14	2	.997	.987	.987	.977	.937	.903	.847	.784
1.99	.465	5020	.14	2	.936	.853	.816	.720	.441	.286	.195	.112
2.45	.114	2150	.15	1	.998	.989	.989	.989	.963	.932	.863	.816
2.50	.224	3790	.14	1	.986	.973	.970	.955	.847	.739	.598	.515
2.45	.114	2280	.15	2	.995	.984	.990	.979	.918	.864	.786	.714
2.45	.224	3950	.15	2	.976	.938	.925	.886	.706	.564	.441	.335

M	$\frac{\rho_\infty}{\bar{\rho}}$	β	δ, ft	$\frac{n}{2}$	E_M/E_o for aperture diameters, dx10³ inch							
					8.09	4.86	4.20	3.32	1.80	1.28	1.01	0.75
(b) Boundary-layer configuration (2); φ = 0°, D = 2.5 in.												
0.41	0.938	780	(1)	2	1.00	1.00	0.998	1.00	1.00	0.975	0.905	0.910
.65	.236	560	---	1	1.00	1.00	.990	1.00	1.00	1.00	.990	.966
.65	.469	1150	---	1	1.00	1.00	1.00	1.00	1.00	.982	.948	.934
.65	.704	1510	---	1	.998	1.00	.992	.999	.974	.941	.863	.823
.64	.936	2080	---	1	.996	.996	.991	.988	.951	.893	.808	.733
.68	.232	630	---	2	1.00	1.00	1.00	1.00	1.00	.994	.942	.942
.68	.457	1210	---	2	.998	1.00	.997	1.00	.969	.929	.847	.820
.68	.686	1810	---	2	.994	.997	.994	.992	.927	.845	.708	.668
.67	.921	2180	---	2	.983	.982	.973	.964	.847	.711	.585	.499
.80	.233	810	---	1	1.00	.998	.994	.995	1.00	.995	.978	.944
.80	.465	1600	---	1	.999	1.00	1.00	1.00	.970	.939	.877	.850
.79	.703	2220	---	1	.995	.985	.992	.983	.947	.871	.780	.700
.79	.936	2940	---	1	.987	.980	.975	.964	.864	.752	.624	.521
.82	.231	750	---	2	.999	.987	.999	.989	.992	.969	.913	.848
.81	.463	1470	---	2	.994	.988	1.00	.989	.958	.872	.760	.687
.80	.696	1970	---	2	.984	.974	.977	.962	.868	.705	.543	.467
.81	.922	2780	---	2	.973	.957	.958	.915	.754	.559	.412	.304
1.43	.112	1120	.33	1	1.00	.995	.995	.995	.984	.960	.931	.916
1.43	.225	2190	.25	1	.998	.987	.981	.974	.952	.901	.836	.802
1.42	.453	3820	.22	1	.989	.978	.967	.965	.880	.767	.651	.564
1.43	.115	1370	.33	2	.985	.973	.968	.965	.960	.940	.903	.835
1.42	.235	2330	.25	2	.993	.977	.976	.960	.912	.860	.756	.662
1.42	.453	3910	.22	2	.976	.938	.927	.888	.713	.554	.448	.330
1.76	.111	1420	.23	1	1.00	1.00	1.00	.993	.970	.950	.918	.904
1.75	.228	2560	.22	1	.991	.975	.973	.975	.917	.808	.687	.606
1.76	.461	5340	.23	1	.968	.928	.907	.881	.682	.481	.354	.255
1.76	.113	1390	.23	2	.996	.992	.988	.974	.948	.892	.830	.749
1.76	.223	2610	.22	2	.985	.957	.963	.945	.828	.708	.578	.484
1.75	.461	5340	.23	2	.945	.858	.834	.756	.465	.306	.214	.137
2.01	.109	1660	.20	1	.998	.993	.988	.988	.971	.936	.887	.841
2.01	.225	2970	.17	1	.987	.977	.971	.959	.891	.762	.642	.523
1.96	.474	5470	.18	1	.958	.911	.885	.816	.573	.396	.286	.189
2.00	.110	1640	.20	2	.995	.990	.977	.978	.937	.886	.795	.716
1.99	.228	3060	.17	2	.980	.958	.947	.909	.753	.611	.481	.385
1.97	.474	5790	.18	2	.931	.827	.770	.677	.376	.246	.156	.102
2.44	.115	2360	.19	1	.996	.992	.989	.984	.945	.896	.817	.734
2.50	.225	4020	.18	1	.978	.955	.941	.919	.751	.597	.481	.361
2.44	.114	2290	.19	2	.990	.976	.972	.965	.883	.806	.687	.581
2.51	.221	4100	.18	2	.962	.920	.890	.851	.599	.435	.306	.212

[1]Channel flow impended for the subsonic Mach numbers for configuration (2). The velocity profiles were given to good approximation by the logarithmic velocity decrement law:

$$\frac{u_\infty - u}{u_\infty} = -\log_{10}\left(\frac{y}{\delta}\right)^{1/m}$$

where δ in this case is the half-width of the wind tunnel (6 in.). The value of m for all the profiles fell in the range

$$5.6 < m < 6.2$$

The lower value is associated with the lowest density ratio ($\rho_\infty/\bar{\rho} = 0.22$).

TABLE IV.- TABULATION OF DATA - Concluded

(c) Boundary-layer configuration ③; φ = 0°, D = 2.5 in.

M	$\frac{\rho_\infty}{\rho}$	β	δ, ft	n/2	E_M/E_o for aperture diameters, dx10³ inch: 8.14	4.71	4.07	3.27	1.85	1.23	1.07	0.71
0.41	0.920	850	0.23	2	1.00	1.00	1.00	0.995	0.991	0.960	0.965	0.955
.66	.458	1030	.21	1	1.00	1.00	1.00	1.00	.982	.965	.970	.925
.66	.458	1030	.21	2	1.00	.999	.997	.995	.975	.946	.931	.876
.69	.677	1590	.20	1	1.00	.995	.995	.990	.950	.910	.896	.850
.69	.677	1590	.20	2	1.00	.995	.990	.983	.920	.835	.803	.696
.66	.920	2040	.21	1	.995	.992	.992	.985	.935	.852	.827	.717
.66	.920	2040	.21	2	.980	.965	.961	.953	.862	.725	.673	.542
.82	.231	720	.20	1	1.00	.995	1.00	1.00	.995	.975	.980	.966
.82	.231	720	.20	2	1.00	1.00	1.00	1.00	.990	.962	.959	.934
.83	.450	1420	.20	1	1.00	1.00	1.00	1.00	.967	.921	.903	.834
.83	.450	1420	.20	2	1.00	.991	.988	.983	.926	.850	.826	.703
.81	.685	2100	.20	1	1.00	.997	.997	.981	.923	.835	.782	.684
.81	.685	2100	.20	2	.983	.969	.962	.943	.816	.660	.623	.470
.82	.904	2840	.20	1	.988	.980	.976	.958	.853	.706	.656	.507
.82	.904	2840	.20	2	.975	.945	.926	.886	.687	.495	.440	.273
1.40	.246	2730	.25	1	.998	.987	.980	.973	.918	.855	.815	.713
1.40	.246	2730	.25	2	.988	.966	.956	.943	.832	.703	.654	.528
1.43	.505	5550	.27	1	.978	.939	.922	.882	.700	.512	.448	.285
1.43	.505	5550	.27	2	.953	.865	.825	.750	.470	.282	.246	.137
1.70	.0970	1510	.21	1	.995	.991	.992	.989	.969	.944	.938	.895
1.70	.0970	1510	.21	2	.995	.989	.985	.982	.952	.888	.877	.818
1.72	.227	3460	.23	1	.990	.973	.966	.957	.882	.788	.733	.595
1.72	.227	3460	.23	2	.990	.957	.941	.916	.750	.598	.540	.388
1.74	.449	6820	.23	1	.956	.900	.872	.819	.573	.388	.325	.191
1.74	.449	6820	.23	2	.918	.801	.737	.629	.336	.192	.152	.090
1.94	.159	2910	.22	1	.988	.982	.982	.973	.924	.856	.824	.718
1.94	.159	2910	.22	2	.980	.975	.960	.938	.843	.716	.677	.522
1.96	.195	3590	.22	1	.986	.970	.965	.951	.875	.784	.731	.580
1.96	.195	3590	.22	2	.973	.940	.930	.904	.751	.592	.530	.376
1.96	.233	4460	.22	1	.986	.963	.955	.934	.822	.685	.640	.468
1.96	.233	4460	.22	2	.962	.918	.899	.854	.658	.456	.411	.266
1.96	.280	5100	.22	1	.978	.951	.938	.910	.754	.602	.543	.378
1.96	.280	5100	.22	2	.948	.886	.855	.796	.559	.353	.310	.181
1.96	.317	5750	.22	1	.971	.934	.914	.875	.700	.516	.448	.309
1.96	.317	5750	.22	2	.939	.860	.822	.738	.469	.298	.242	.139
1.96	.375	6630	.22	1	.962	.904	.875	.818	.601	.406	.342	.214
1.96	.375	6630	.22	2	.922	.808	.744	.654	.363	.201	.158	.097
1.97	.420	7800	.23	1	.953	.876	.838	.772	.498	.318	.259	.140
1.97	.420	7800	.23	2	.898	.743	.673	.558	.278	.146	.115	.065
1.96	.496	9040	.23	1	.935	.835	.773	.683	.402	.238	.191	.105
1.96	.496	9040	.23	1	.848	.652	.569	.452	.194	.098	.076	.039
2.45	.112	3500	.25	1	.986	.981	.979	.971	.932	.859	.816	.719
2.45	.112	3500	.25	2	.975	.961	.956	.937	.836	.722	.647	.523
2.45	.224	6740	.26	1	.969	.933	.913	.876	.692	.511	.443	.296
2.45	.224	6740	.26	2	.939	.860	.815	.736	.483	.296	.238	.135

(d) Boundary-layer configuration ③; φ = 45°, D = 2.5 in.

.82	.231	720	.20	2	.995	.985	.985	.980	.959	.920	.911	.842
.82	.459	1400	.20	2	.971	.963	.961	.952	.875	.770	.712	.593
.81	.694	2120	.20	2	.974	.953	.943	.903	.758	.568	.503	.322
.80	.926	2700	.20	2	.976	.934	.918	.871	.645	.459	.406	.218
1.40	.241	2690	.26	2	.971	.927	.906	.854	.617	.423	.363	.212
1.41	.479	5140	.28	2	.905	.717	.651	.512	2.55	.137	.105	.055

(e) Boundary-layer configuration ③; φ = 0°, D = variable

M_∞	$\frac{\rho_\infty}{\rho}$	δ, ft	n/2	E_M/E_o for aperture diameters, dx10³ inch: 8.14	4.71	4.07	3.27	1.85	1.23	1.07	0.71	D
2.45	0.215	0.25	1	0.940	0.858	0.813	0.746	0.466	0.298	0.246	0.142	2.50
2.45	.215	.25	1	.953	.866	.826	.759	.465	.291	.239	.140	1.75
2.45	.215	.25	1	.940	.855	.806	.744	.465	.290	.254	.144	1.22

(f) Boundary-layer configuration ④; φ = 0°, D = 2.5 in.

M	$\frac{\rho_\infty}{\rho}$	β	δ, ft	n/2	E_M/E_o for aperture diameters, dx10³ inch: 8.09	4.86	4.20	3.32	1.80	1.28	1.01	0.75
0.403	0.926	1225	0.25	2	0.998	---	---	0.998	0.958	0.923	0.891	0.800
.68	.228	830	.23	1	1.00	1.00	1.00	1.00	.985	.975	.958	.944
.68	.457	1960	.23	1	.998	.995	.998	.999	.967	.926	.880	.823
.69	.680	2920	.23	1	.993	.995	.993	.989	.921	.840	.749	.657
.67	.915	3870	.23	1	.988	.984	.978	.973	.887	.785	.655	.547
.68	.228	830	.23	2	.999	.995	.999	.999	.984	.953	.925	.872
.68	.457	1960	.23	2	.994	.984	.984	.979	.932	.852	.782	.686
.69	.680	2920	.23	2	.983	.971	.961	.954	.831	.698	.589	.443
.67	.915	3870	.23	2	.973	.947	.941	.929	.715	.516	.397	.299
.83	.214	1050	.23	1	1.00	.996	.994	1.00	.988	.964	.937	.906
.82	.457	2250	.23	1	.995	.993	.984	.989	.933	.863	.783	.697
.81	.690	3300	.23	1	.984	.965	.957	.941	.846	.702	.577	.469
.81	.924	4440	.23	1	.974	.953	.937	.901	.721	.554	.417	.315
.83	.214	1050	.23	2	.998	.994	1.00	.990	.967	.929	.870	.816
.82	.457	2250	.23	2	.988	.977	.974	.969	.882	.766	.657	.541
.81	.690	3300	.23	2	.970	.954	.948	.894	.678	.519	.392	.276
.81	.924	4440	.23	2	.946	.885	.865	.794	.512	.345	.239	.139
1.34	.238	3520	.26	1	.986	.971	.962	.958	.865	.744	.629	.505
1.36	.461	6960	.24	1	.952	.911	.881	.839	.555	.389	.257	.163
1.33	.238	3460	.26	2	.974	.957	.940	.909	.741	.588	.446	.301
1.35	.468	6980	.24	2	.970	.858	.799	.676	.332	.196	.116	.077
1.69	.120	2210	.23	1	.997	.992	.985	.981	.957	.917	.820	.773
1.76	.216	4260	.23	1	.984	.964	.949	.938	.818	.692	.544	.452
1.73	.455	8250	.22	1	.935	.851	.761	.718	.416	.271	.172	.110
1.69	.119	2210	.23	2	.991	.985	.984	.963	.894	.812	.694	.615
1.75	.220	4290	.23	2	.966	.917	.905	.843	.619	.444	.334	.240
1.73	.455	8250	.22	2	.894	.728	.652	.524	.229	.129	.080	.053
1.73	.463	8390	.22	2	.882	.710	.637	.508	.226	.128	.078	.043
1.92	.116	2780	.25	1	.993	.989	.986	.975	.929	.868	.755	.660
1.92	.230	5570	.25	1	.978	.951	.944	.921	.749	.581	.447	.360
1.90	.460	11100	.25	1	.917	.810	.752	.658	.376	.219	.136	.078
1.92	.117	2780	.24	2	.986	.976	.969	.947	.846	.738	.616	.509
1.92	.232	5620	.25	2	.953	.895	.866	.775	.499	.344	.242	.161
1.90	.463	11200	.25	2	.861	.637	.561	.415	.162	.087	.052	.028
2.42	.119	4470	.28	1	.990	.978	.969	.934	.891	.782	.676	.580
2.42	.240	9140	.28	1	.957	.911	.892	.837	.563	.388	.264	.185
2.41	.122	5580	.28	2	.977	.958	.956	.914	.744	.574	.433	.346
2.42	.237	9030	.28	2	.918	.800	.754	.650	.340	.185	.126	.079

(g) Boundary-layer configuration ④; φ = 45°, D = 2.5 in.

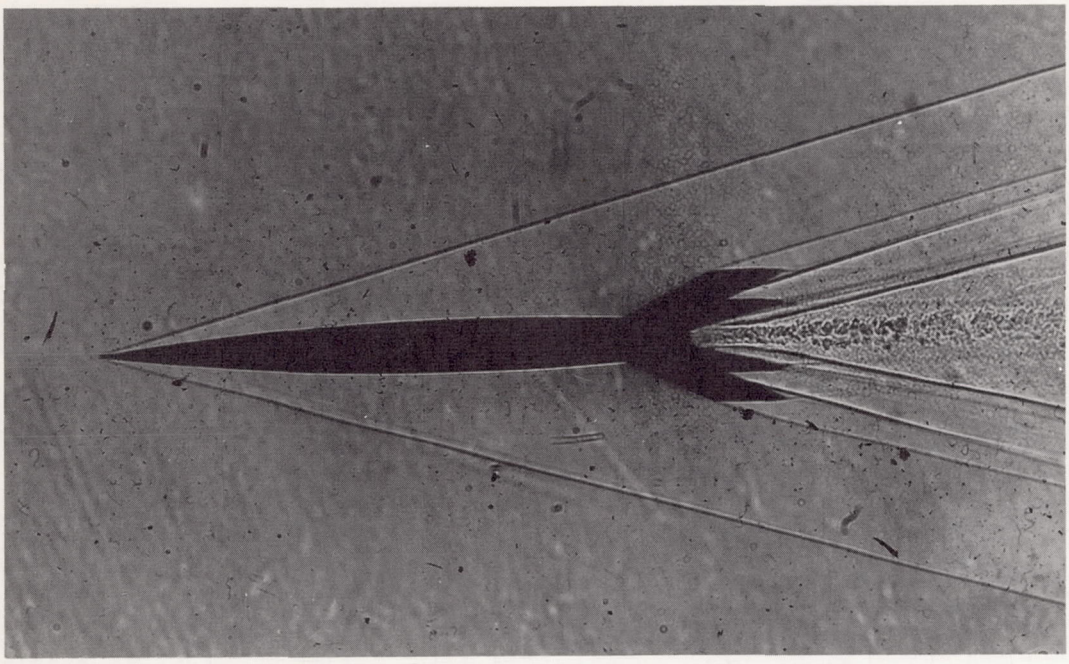
.82	.225	1080	.23	2	.997	.996	.993	.992	.954	.914	.849	.772
.82	.456	2210	.23	2	.978	.968	.955	.930	.764	.630	.495	.368
.82	.690	3320	.23	2	.963	.932	.918	.862	.599	.428	.334	.215
.82	.918	4530	.23	2	.929	.853	.815	.708	.407	.256	.172	.098
1.39	.227	3440	.26	2	.955	.911	.882	.817	.537	.390	.274	.173
1.37	.455	6970	.24	2	.886	.665	.581	.439	.178	.100	.073	.046

(h) Boundary-layer configuration ⑤; φ = 0°, D = 2.5 in.

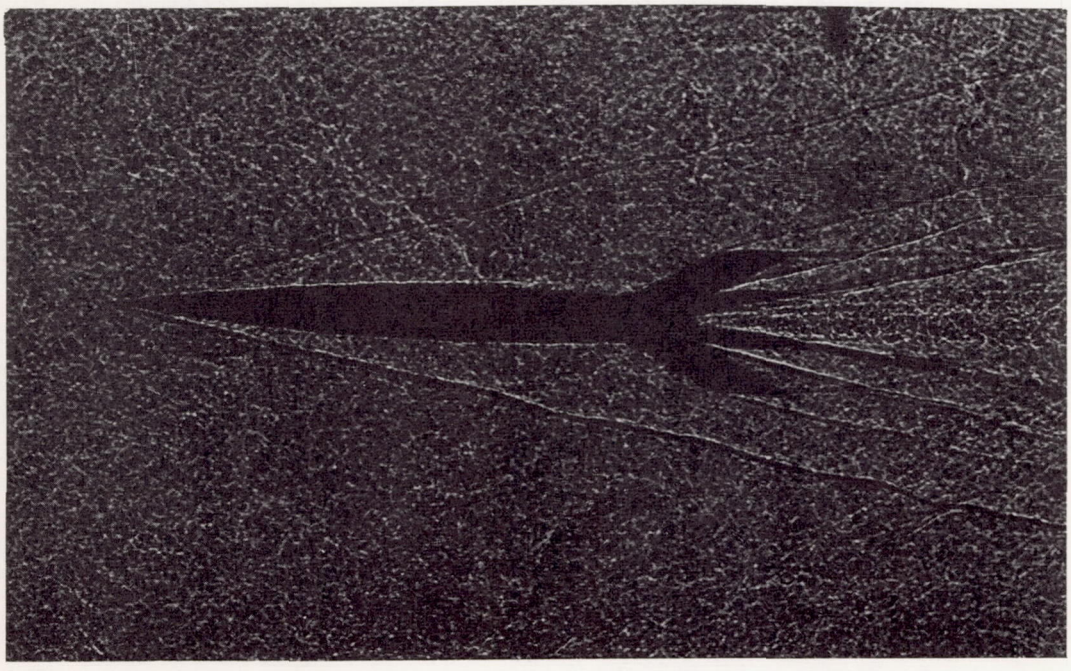
M	$\frac{\rho_\infty}{\rho}$	δ_{sep}, ft	δ, ft	β	n/2	E_M/E_o for aperture diameters, dx10³ inch: 8.09	4.86	4.20	3.32	1.80	1.28	1.01	0.75
1.33	0.192	0.035	0.26	4620	1	0.987	0.983	0.976	0.971	0.878	0.795	0.620	0.513
1.33	.191	.030	.23	4100	2	.968	.946	.931	.899	.708	.488	.374	.251
1.22	.407	.080	.24	9150	1	.935	.873	.842	.763	.468	.286	.182	.110
1.22	.407	.080	.26	9400	2	.887	.742	.684	.551	.242	.137	.078	.047

(i) Boundary-layer configuration ⑥; φ = 0°, D = 2.5 in.

M	$\frac{\rho_\infty}{\rho}$	δ_{sep}, ft	δ, ft	β	n/2	E_M/E_o for aperture diameters, dx10³ inch: 8.14	4.71	4.07	3.27	1.85	1.23	1.07	0.71
1.23	0.213	0.04	0.30	5300	1	0.991	0.980	0.972	0.955	0.838	0.690	0.603	0.427
1.23	.213	.04	.30	5300	2	.988	.960	.939	.881	.648	.460	.370	.222
1.27	.439	.07	.30	12150	1	.952	.850	.776	.680	.342	.197	.161	.079
1.27	.439	.07	.30	12150	2	.885	.672	.552	.431	.174	.087	.069	.032



(a) Tunnel Mach number = 0; missile Mach number = 4



(b) Tunnel Mach number = 2; missile Mach number = 5

Figure 1.- Shadow photographs of missile models in the Ames supersonic free-flight wind tunnel showing the effect of turbulent layers on a collimated light beam; spark duration 0.5 microsecond.

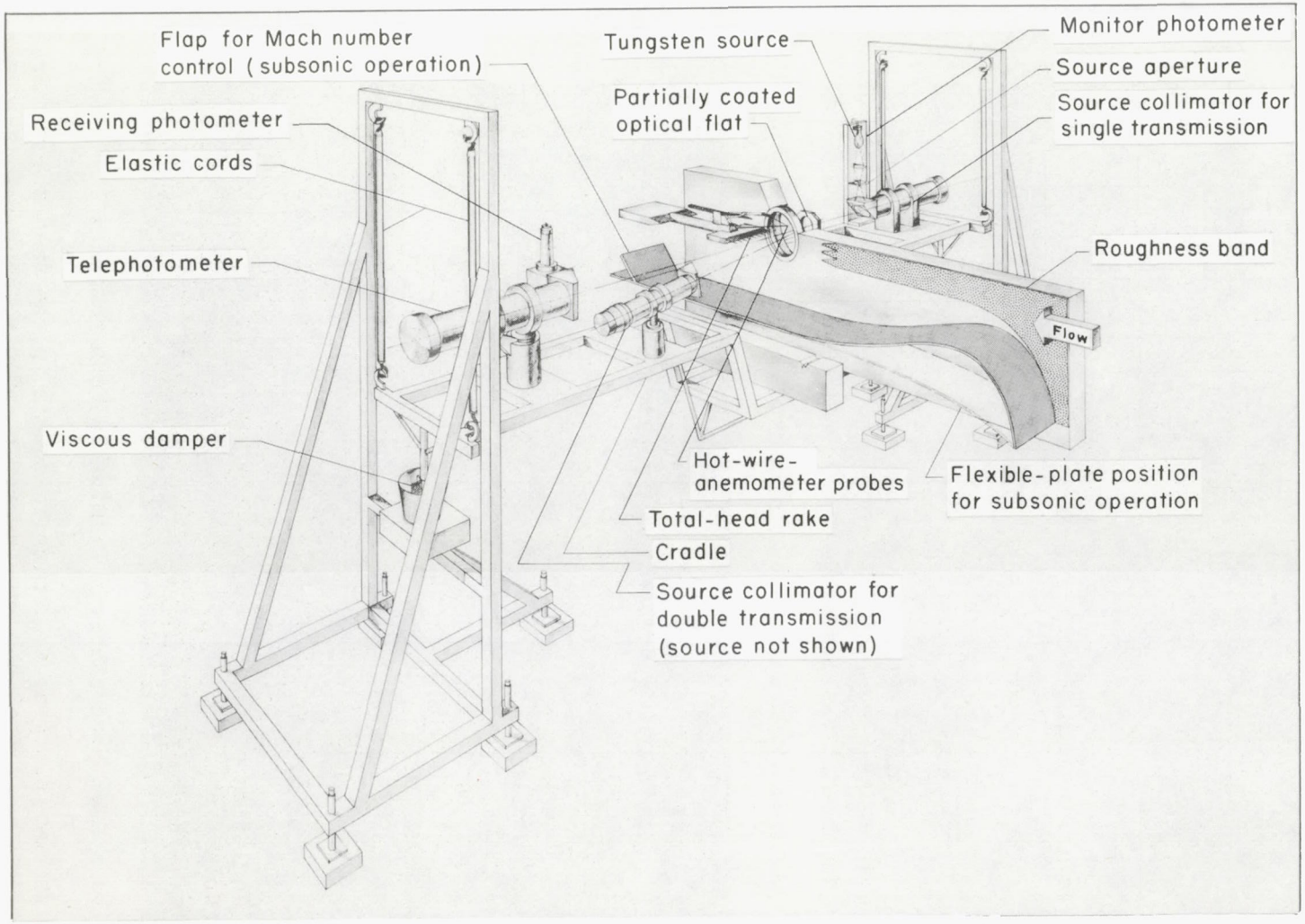


Figure 2.- Experimental arrangement for viewing a point light source at infinity through two or four thickened turbulent wall boundary layers in the Ames 1- by 3-foot supersonic wind tunnel no. 1.

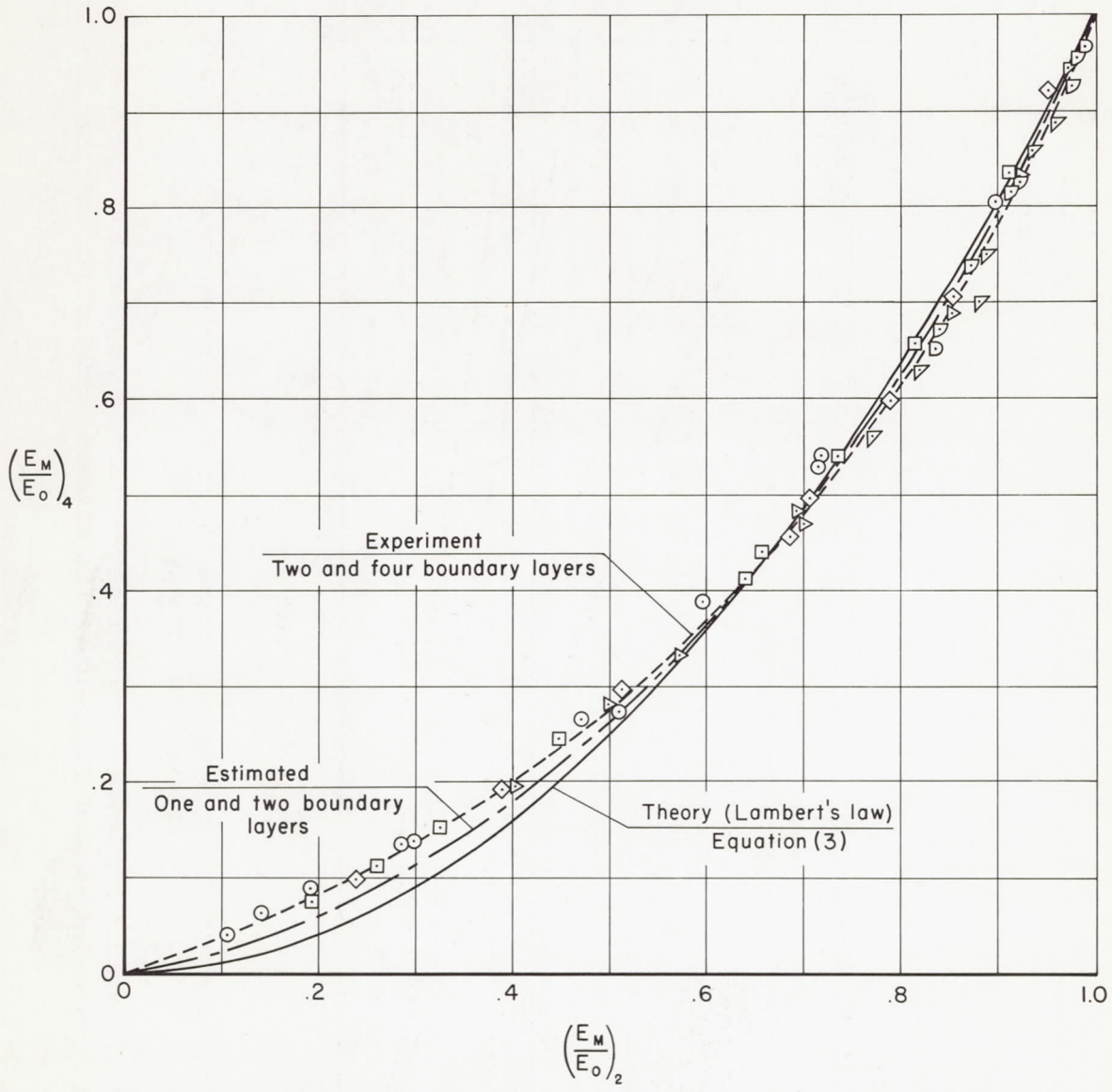
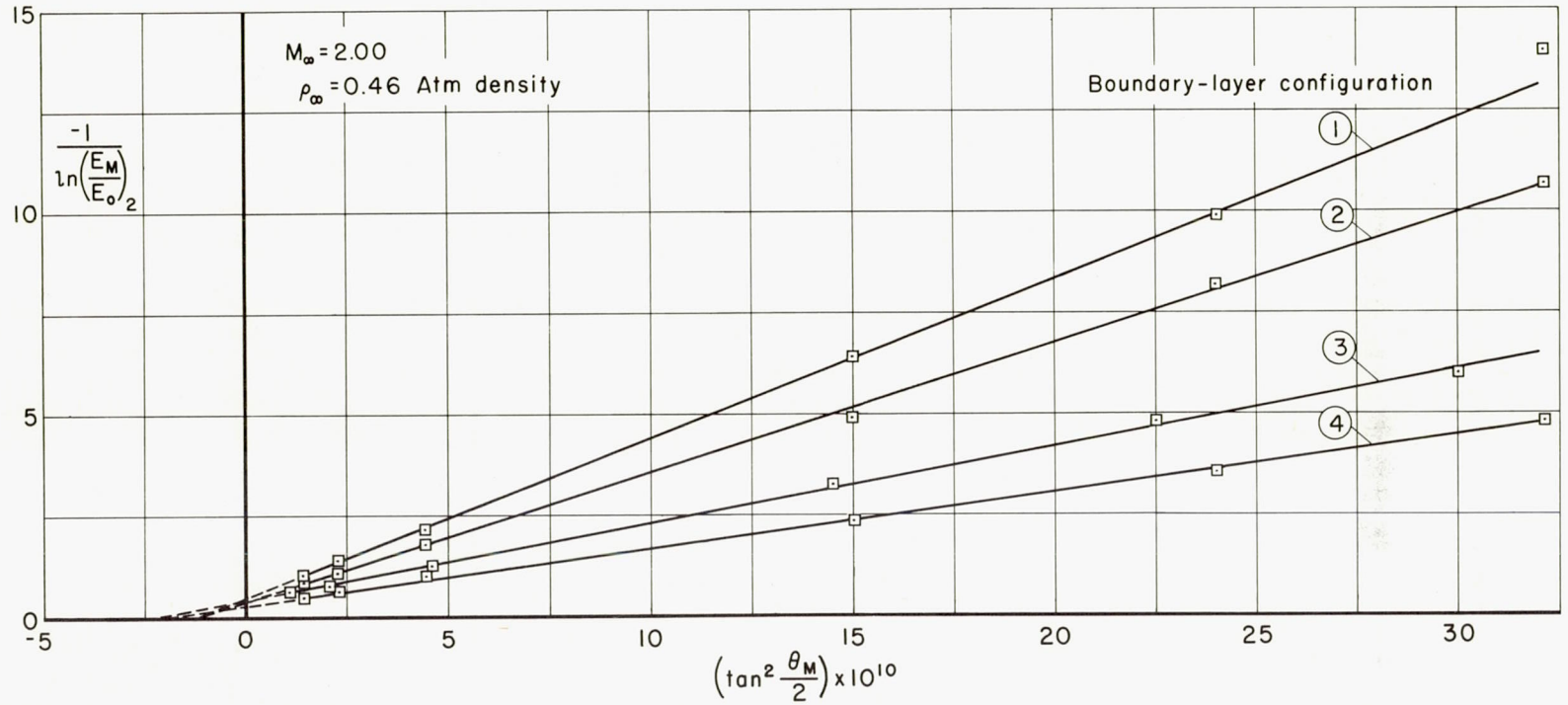
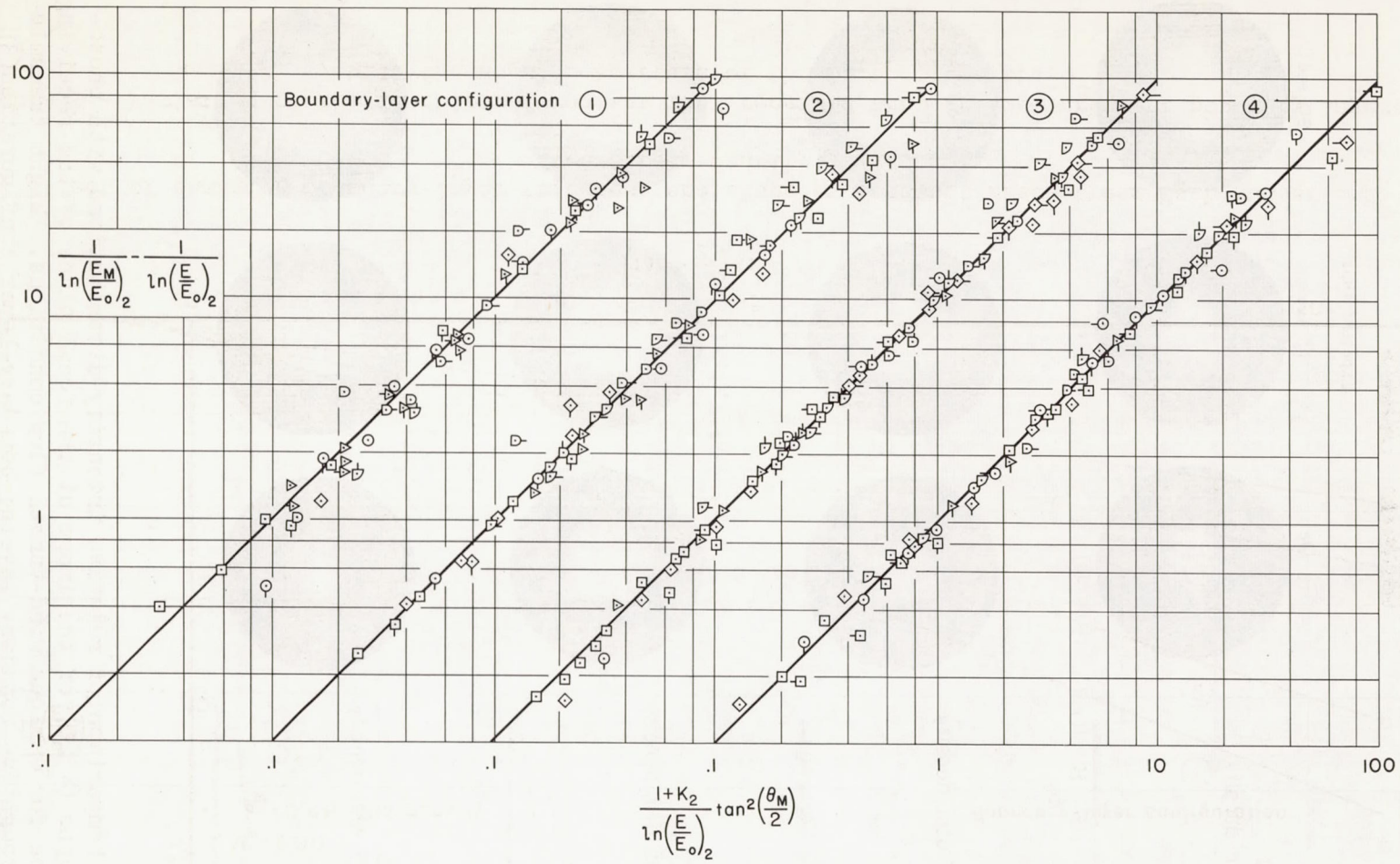


Figure 3.- Variation of the fraction of radiant flux received through four turbulent boundary layers with the fraction received through two. Boundary-layer configuration (3). (See table I for symbol identification.)



(a) Effect of changing boundary-layer thickness and shape at constant free-stream Mach number and free-stream density.

Figure 4.- Variation of the fraction of radiant flux received through two turbulent boundary layers with the angular aperture of the telephotometer.



(b) Correlation of data for various Mach numbers and densities employing parameters predicted by scattering theory. (See table II for symbol identification.)

Figure 4.- Concluded.

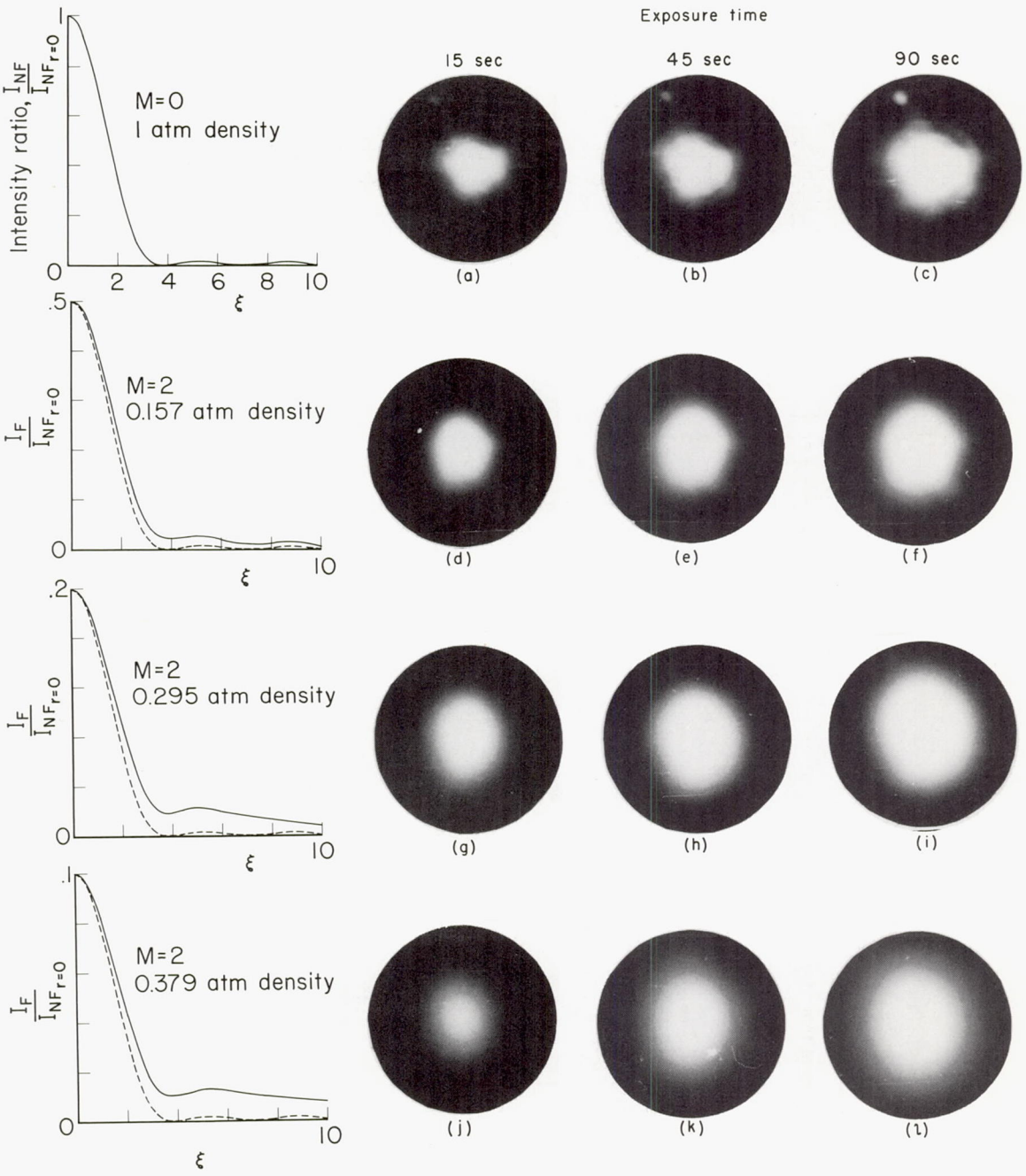


Figure 5.- Comparison of relative intensity distributions with photomicrographs (×320) of the image at the focal plane of the receiving telescope for various wind-tunnel flow conditions. Light transmission through two boundary layers; boundary-layer configuration (3).

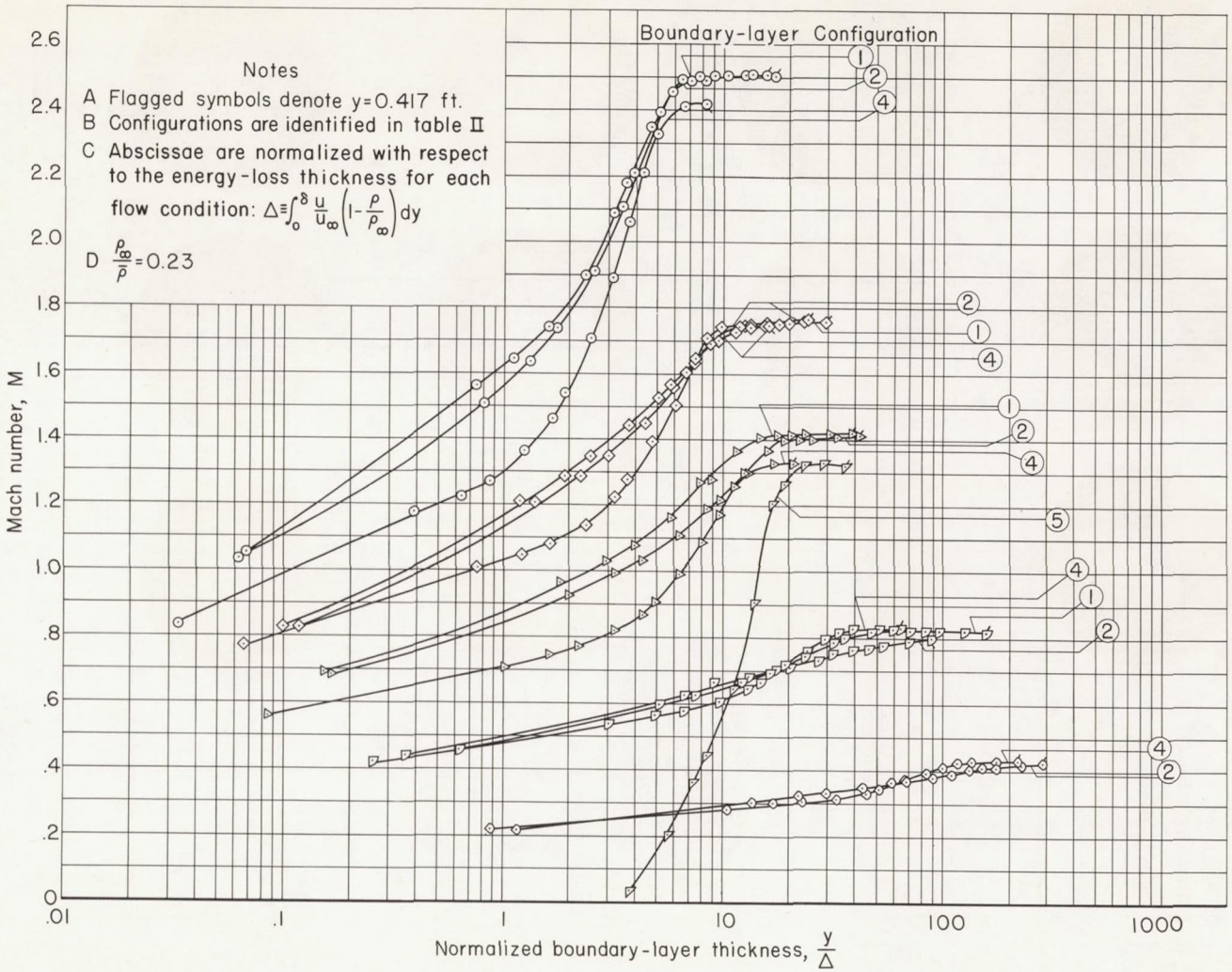


Figure 6.- Effect of various methods for thickening turbulent boundary layers on the shape of the Mach number profiles.

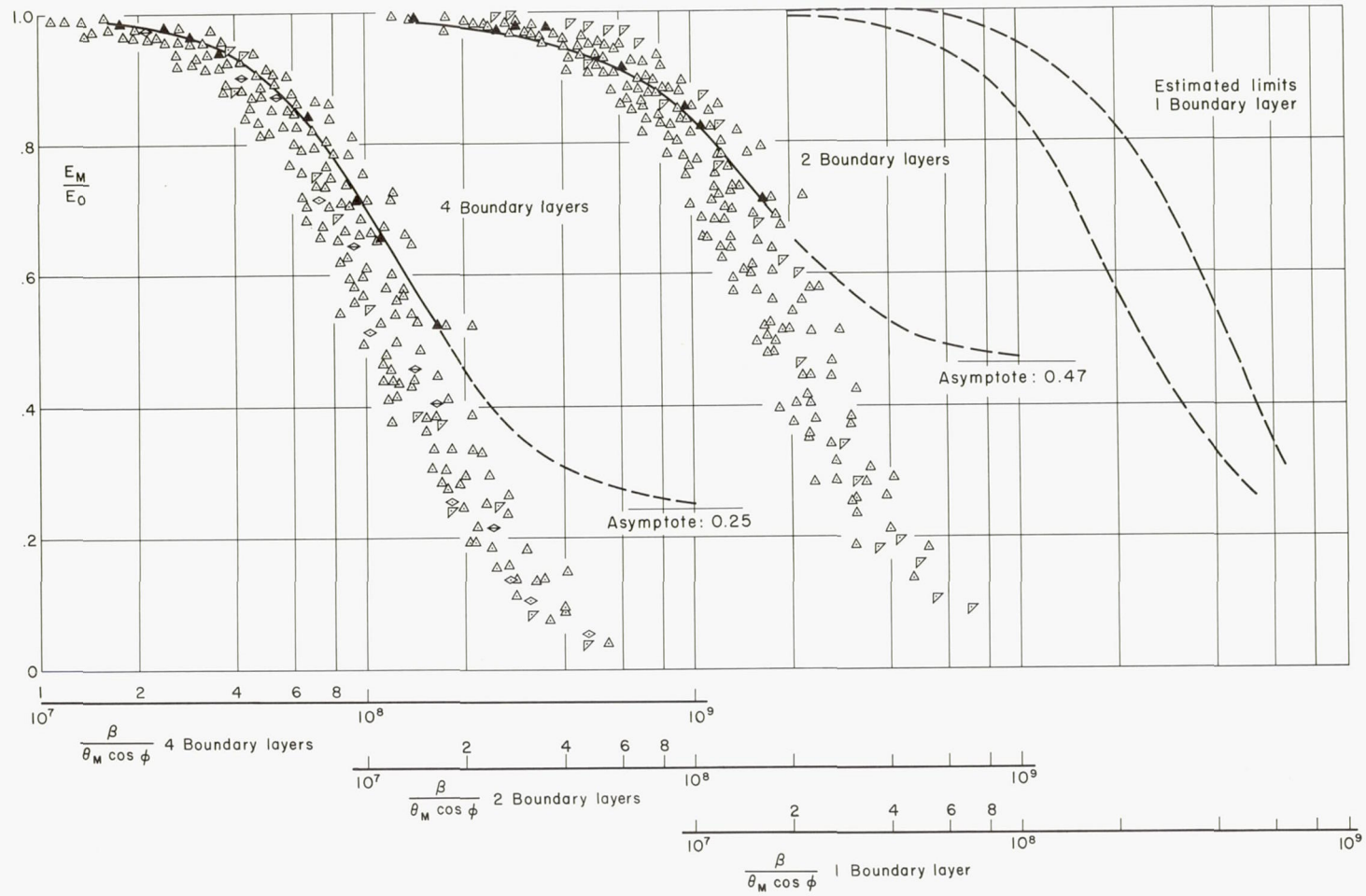


Figure 7.- Attenuation of radiant flux through one, two, and four turbulent boundary layers as a function of the combined mean flow and optical parameter, $\beta/\theta_M \cos \varphi$. (See tables II and III for symbol identification.)